The influence of crystallinity on the properties of carbon nanotubes

Mattias Flygare

The influence of crystallinity on the properties of carbon nanotubes

Mattias Flygare

The influence of crystallinity on the properties of carbon nanotubes

Mattias Flygare

DOCTORAL THESIS

WWW.KAU.SE

Abstract

Carbon nanotubes have been advertised as a material with quite extraordinary properties, both mechanically and electrically. The truth is that carbon nanotubes is not one material, but several different. Depending on the method used to produce them, and consequently the quality of the atomic structure within their walls, their physical properties can also differ drastically.

In this doctoral thesis a method was developed for quantifying the degree of order within the tubes' walls, namely their crystallinity, by using transmission electron microscopy. The method enables the characterization of the inherent properties of the tubes such as electrical conductivity and bending stiffness, alongside the determination of crystallinity, making it possible to quantify the influence of tube crystallinity on these critical properties. Furthermore, a model for electrical conduction in the outermost wall of multi-walled carbon nanotubes is suggested, enabling the determination of intrinsic quantities like the sheet resistance of individual crystallite grains within the walls and the boundaries in-between them.

The studies reveal a profound shift in both mechanical and electrical behavior at a critical crystallite size, with large differences connected to production method, and even between individual tubes from the same production batch. These findings successfully explain previously seen differences and highlight the need for well-defined characterization techniques with protocols and classification systems, in order to successfully exploit the promising properties of carbon nanotubes in the future.

List of publications

The dissertation includes the following publications.

I *Quantifying crystallinity in carbon nanotubes and its influence on mechanical behaviour.* Mattias Flygare and Krister Svensson, Materials Today Communications, 18:39–45, 2019.

II *Accurate determination of electrical conductance in carbon nanostructures.* Mattias Flygare and Krister Svensson, In preparation for submission to Measurement Science and Technology (manuscript), 2021.

III *Influence of crystallinity on the electrical conductivity of individual carbon nanotubes.* Mattias Flygare and Krister Svensson, Carbon Trends, 5:100125, 2021.

IV *Effects of high temperature treatment of carbon nanotube arrays on graphite: increased crystallinity, anchoring and inter-tube bonding.* Josef Hansson, Andreas Nylander, Mattias Flygare, Krister Svensson, Lilei Ye, Torbjörn Nilsson, Yifeng Fu and Johan Liu. Nanotechnology, 31(45):455708, 2020.

V *Hierarchical cellulose-derived CNF/CNT composites for electrostatic energy storage.* Volodymyr Kuzmenko, Muhammad Amin Saleem, Henrik Staaf, Mazharul Haque, Arun Bhaskar, Mattias Flygare, Krister Svensson, Vincent Desmaris and Peter Enoksson, Journal of Micromechanics and Microengineering, 26(12), 2016.

Contributions

The author of this dissertation was responsible for most of the writing and carried out all of the experimental work and analysis in publications I, II and III. In publication IV the contribution from the author was using the method developed in I to take measurements of carbon nanotube crystallinity, the analysis thereof, as well as writing a part of the publication. In publication V the contribution from the author was a qualitative TEM analysis of the carbon nanotube/fiber samples in the study, and writing part of the publication.

Publications not included in this dissertation

- *Cellulose-derived carbon nanofibers/graphene composite electrodes for powerful compact supercapacitors.* Volodymyr Kuzmenko, Nan Wang, Mazharul Haque, Olga Naboka, Mattias Flygare, Krister Svensson, Paul Gatenholm, Johan Liu and Peter Enoksson, RSC Advances, 7(73), 2017.
  https://doi.org/10.1039/C7RA07533B.

Acknowledgments

List of acronyms

CNT carbon nanotube
CVD chemical vapor deposition
EBID electron beam induced depositions
FWHM full width at half maximum
SWCNT single-walled carbon nanotube
MWCNT multi-walled carbon nanotube
SAED selected area electron diffraction
SEM scanning electron microscope
STM scanning tunnelling microscope
TEM transmission electron microscope
XRD X-ray diffraction

Contents

Chapter 1
Introduction

A carbon nanotube (CNT) is a tube made of carbon. It is astonishingly small, as nano refers to the billionth of one meter that is the closest unit of length that is practical to use when sizing up their diameter. Carbon nanotubes can also be thought of as a material, with material properties, many of which are expected to be very useful in a wide variety of applications. The unusually good behavior of CNTs that has been promised, calculated and theoretically predicted, stems from the atomic structure within the nanotube walls, giving them for example high mechanical stiffness [1] and electrical conductivity [2]. As the theoretical values for such beneficial properties are based on an ideal atomic structure, one is right to ask the questions *"what happens when the atoms are not as well ordered?"* and *"what conditions of growth lead to a well ordered structure?"*.

Indeed, defects in the atomic lattice have been found to influence the mechanical stiffness [3, 4, 5], tensile strength [6, 7], and the whole mechanical behavior in bending configurations [8, 9]. The thermal conductivity [10, 11] has also been found to depend on the order/disorder within the tube walls. Theoretically, some types of CNT may have an electrical resistance that is close to zero, regardless of the length of the tube, however these properties have also been found to deteriorate as the tubes differ from the idealized versions of themselves [12, 13]. For nanotubes grown by the method of arc-discharge, which is believed to be one of the best methods for producing high quality tubes, the electrical current has been found to be carried by the outermost layer for distances of up to about 1 μm [14], while for tubes grown with chemical vapor deposition (CVD) the electron mean free path has been found to be very short, even below 10 nm [15], showing that tubes from the two different methods of production may differ in quality.

1

While it may be obvious that different techniques of production can produce different results, there are also large differences in behavior found within the same methods, and even within the same sample batches of CNT, further showing how sensitive these properties are to how well ordered their atoms are, referred to as the "crystallinity" of the tubes. In electrical measurements of CNTs using four electrical probes there are reports of 0.2–86 kΩ/µm [16], 1.4–10.4 kΩ/µm [17] and 6–25 kΩ/µm [14], without any apparent cause for the large differences, even within the same experimental set-up. Another study which used two-probe measurements found similar variations in the linear resistance and a large spread of about two orders of magnitude in the estimated band gaps of semiconducting tubes [18].

The conclusion then is quite clear; "carbon nanotubes" is not a single material, it is several, and the properties and possible benefits that they may bring is highly dependent, and sensitive of, the quality of their atomic lattice structure and indirectly their method of production. Characterization of commercially available carbon nanomaterials reveal large differences within CNTs sold under the same description [19], and the future exploitation of nanotubes thereby relies on well defined characterization techniques with protocols [20] and classification systems [21, 22], similar to the ones that have been established for carbon fibers [23].

For the work described in this dissertation there was a need for an in-situ method to quantify nanotube crystallinity simultaneously, or in the same session, as measuring other properties. Techniques for measuring bending stiffness inside a transmission electron microscope (TEM) were already in place and methods for electrical characterization were being planned. This led to the development of a new technique that would accomplish all this, with reasonable ease-of-use and accuracy. The method relies on using selected area electron diffraction (SAED) inside a TEM and an analysis of the diffraction pattern in terms of peak width. The method is similar to X-ray diffraction (XRD) and previous TEM diffraction schemes, but manages to eliminate the influence of streaking and instrument contributions so that the inherent peak broadening from a limited crystallinity can be accessed. Great care has been taken to correct for different contributions to line-broadening [24], which includes

taking into account the specific shape and orientation of the studied structure when analyzing its corresponding diffraction image, in a way that has not been reported before. The work also includes a detailed mapping of the most important instrument contributions for these measurements so that these could be properly adjusted and corrected for.

The methods described above were also put into practice, and some very interesting results were found within this work. The differences found in the mechanical properties of CNTs produced with different methods [9, 25], are here linked to large differences in crystallinity. For arc-discharge tubes, the in-plane crystallite size L_a was found to be on the order of 20 nm while for CVD growth it was only about 5 nm. The findings successfully explain the previously seen differences in for example bending stiffness, and highlight the sensitivity of differences in crystallinity, and indirectly of production method.

A profound effect from a limited crystallinity was also found in electrical conductivity, and is presented in this dissertation. Within the same batch of arc-discharge CNTs, the linear resistance was found to vary from 3–300 kΩ/µm, directly correlated to the effective size of the crystallites. Furthermore, a model is presented where the conduction is described by modeling the outermost tube layer as polycrystalline graphene, with individual graphene grains with a sheet resistance, connected via grain boundaries, with a boundary resistivity. Values are extracted for these parameters and it is shown that both of these depend critically on the crystallite size. For smaller crystallite sizes below about 10 nm, the current jumps from grain to grain, crossing relatively resistive boundaries. For higher crystallite sizes the sheet resistance within each grain becomes very low, comparable to a ballistic behavior, and is limited by scattering at the grain boundaries. These differences are interpreted as a combination of quantum confinement and edge effects in the individual crystallites which dominate the behavior for smaller grain sizes.

A detailed description of both the methods that were developed, as well as the unique results on carbon nanotubes that they helped discover, can be found throughout the rest of this dissertation and in the publications from which it builds.

Chapter 2
Background

2.1 Carbon nanotubes

Although the question if carbon nanotubes appear "naturally" is still not completely settled at the time of writing this dissertation, there is no question that things that are like CNT have been observed as early as the 19th century, for example as accidental byproducts of industrial processes or similar hot sources. In the mid 1900s there began surfacing evidence as actual pictures of tubular structures made from carbon atoms, due to the invention of the transmission electron microscope [26]. It was in 1991 that Iijima famously "discovered" carbon nanotubes [27], and when multi-walled carbon nanotubes (MWCNTs) were first introduced to the wider scientific community, followed by single-walled carbon nanotubes (SWCNTs) a couple of years later.

Theoretical models of CNT have also predicted spectacular properties, mechanical, electrical and thermal. Some of these predictions have been experimentally confirmed, or at least approximated, while others have not. The sensitivity of the exact placement of each atom in the structure, i.e. the crystallinity, has however proved to be very high, and in many cases the presence of small defects may drastically alter the tubes' physical properties.

2.1.1 Atomic structure

The material of CNTs is closely related to the material graphene, well known for rendering a Nobel prize in 2010. Graphene is a sheet of carbon atoms which is one atom thick, and thus is referred to as a two-dimensional material. Within the plane of the sheet the atoms are ordered in a hexagonal pattern, which calculations show gives it quite magical properties, when combined with

the thinness of the material and the inherent properties of the carbon atoms from which the lattice is formed. This is in essence due to the super strong covalent bonds between the atoms in the plane, formed by the so called sp^2 hybridization of the electron orbitals. These bonds, which are all in one plane with a 120° angle between them, are even stronger than the four bonds of each carbon atom found in diamond, where the orbitals instead mix with sp^3 hybridization. Moreover, the "missing" fourth bond of each atom in graphene compared to the diamond crystal structure instead all combine into one big orbital on each side of the graphene plane, where the electrons can move freely, giving graphene its remarkable electrical properties. For a more detailed and accurate description of the structure of carbons and their emergent properties, see for instance references [28] or [29]. For graphene, similarly to CNTs, experiments have shown that some of these properties are so far achievable in real-life applications, while some require an as of yet unrealistic order within the atomic lattice structure.
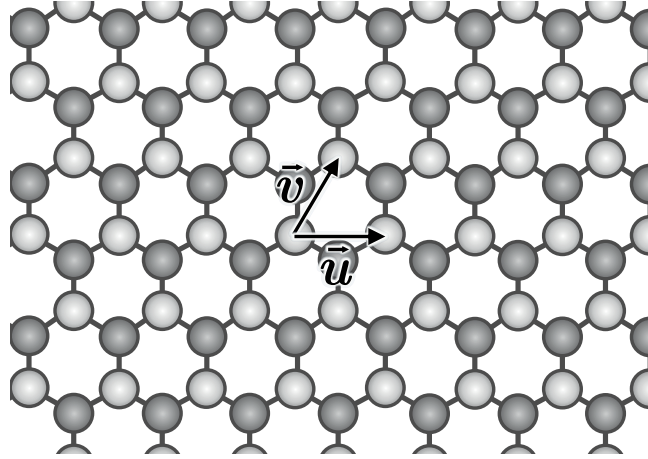
Figure 2.1: A sheet of graphene with the base vectors $\vec{u}$ and $\vec{v}$ pointing to the two nearest neighboring atoms of the same bond rotation.

The walls of CNTs are also one atom thick and, just like graphene, consist of an hexagonal lattice of carbon atoms within the plane of the walls, which is why it is natural to think of SWCNTs as a sheet of graphene rolled up into a cylinder, and MWCNTs as several of these cylinders of different diameters stacked inside each other.

The question now becomes how the graphene sheets are "glued" together

when the bent up sheet joins itself to form a cylinder, a property known as the tube's "chirality". It turns out there are several ways this can happen theoretically, but to explain how we must first set up some terminology. Considering the schematic of a sheet of graphene in figure 2.1 we can see how every carbon atom has three bonds to neighboring atoms. Notice that some atoms have a bond pointing straight up, and some have a bond pointing straight down, and we mark them as light or dark in order to distinguish the two possible rotations. We may now define a vector $\vec{u}$ from a light[1] atom to its closest neighbor (in any direction), and a vector $\vec{v}$ from the same atom but to another one of its closest neighbors. The vectors $\vec{u}$ and $\vec{v}$ are called the "base vectors" describing graphene as a hexagonal lattice with two base atoms, one light and one dark, and an example of such a choice of vectors is also shown in figure 2.1.

Now we imagine slicing a CNT open straight along its length, so it becomes a narrow strip of graphene, and we place that strip on top of our previous sheet, rotating the strip until it perfectly lines up with the hexagonal pattern from before. Starting from an atom that is exactly on the edge of one side of the strip, where we sliced the tube apart, we can define another vector $\vec{A}$, that points to the position that the atom would have on the other side of the strip, where the strip's edges previously joined up, shown in figure 2.2.
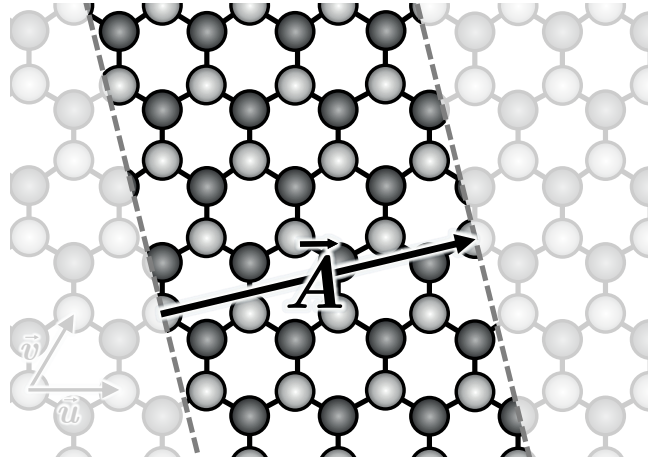
Figure 2.2: A sliced carbon nanotube placed on top of the graphene sheet, with the vector $\vec{A}$ going from an atom on the edge to it's alternate placement on the other edge.

The vector $\vec{A}$ is called the "chiral vector" of the tube, and it defines how the

---

[1]Note that using dark atoms would be an equivalent definition of the vectors.

tube is rolled up, its chirality. Now notice that we can also start from the same atom on the edge and reach the other edge, simply by moving along the vectors $\vec{u}$ and $\vec{v}$ some number of times, in this case three times $\vec{u}$ and one times $\vec{v}$, as shown in figure 2.3.
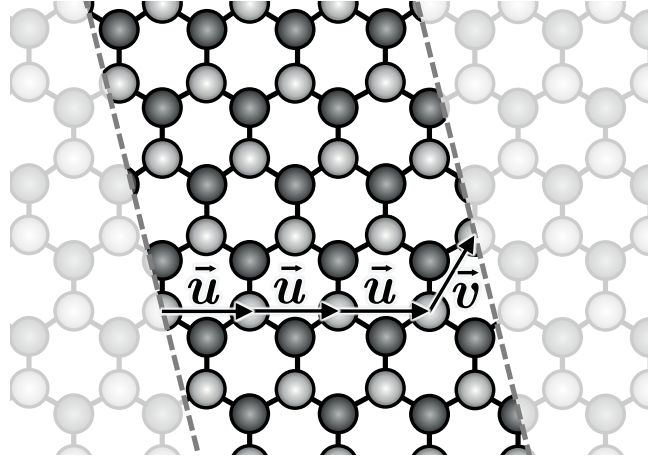
Figure 2.3: A sliced carbon nanotube placed on top of the graphene sheet. Here, a linear combination of the base vectors $\vec{u}$ and $\vec{v}$ going from an atom on the edge to it's alternate placement on the other edge.

Thus we can redefine the chiral vector in terms of the base vectors, as

$$\vec{A} = n \cdot \vec{u} + m \cdot \vec{v}, \tag{2.1}$$

where n and m are integers. These integers equivalently define the tube's chirality, and are usually called the "chiral indices" of the tube, denoted (n, m). Tubes with chiral indices $n = m$ or where either n or m is zero are actually not chiral at all (since they are identical to their mirror image) and these two types are usually called "arm-chair" and "zig-zag" respectively, due to the shape of the atoms when looking at the tube from the side.

As the reader might imagine, the different possibilities for rolling up graphene into tubes does not allow for arbitrary values of tube circumference, since the atoms must line up in specific ways. The circumference of a SWCNT is thereby uniquely determined by its chiral indices (n, m), and its corresponding

diameter d_o can be approximated by

$$d_o \approx 0.783 \cdot \sqrt{(n+m)^2 - nm},\qquad(2.2)$$

measured in nanometers.

The analogous model of a MWCNT is similar to the SWCNT picture, but with multiple cylinders stacked inside each other. There are now additional constrains due to the semi-fixed distance between graphene layers. In graphite, which is a long known and well mapped out material, the individual sheets are actually sheets of graphene, making MWCNT to SWCNT as is graphite to graphene. The analogy is not perfect however, partly since the layers of graphite usually follow very specific "stacking orientations", while the walls of a MWCNT has shown to be "turbostratic", which means the layers of the graphite are not stacked properly, but misaligned by some arbitrary angle. This also has an effect on the typical between-wall distance in MWCNTs which has been shown to be slightly larger than the between-layer distance in graphite, and also has some dependence on the tube's diameter [30].

2.1.2   Production methods

As we have previously touched upon, CNTs can be produced by different methods. The tubes used in this dissertation were produced by two methods: arc-discharge and chemical vapor deposition (CVD).

Arc discharge was the method used by Iijima in 1991 when he first discovered MWCNTs [27], and is among the most common methods. The tubes produced by arc-discharge vary in length and diameter but are of high quality, with few defects. An electric arc plasma is generated between two carbon electrodes, vaporizing the anode at temperatures of 3000–4000 °C, and the tubes self-assemble at the cathode [31, 32]. The tubes are then collected and separated from other carbon materials produced in the process.

The CVD method shows the most promise for industrial-scale production due to its low cost. The nanotubes can also be grown directly on a substrate, skipping the collection process that is necessary with arc-discharge. The substrate

is prepared with metal catalyst particles, which can be used to control the tube diameters. At about 700–800 °C, the substrate is exposed to gasses, a processing gas and a carbon-carrying gas, and nanotubes are formed, starting from the catalyst particles [32]. The tubes can also be purified from their catalyst particles, and thermally annealed to improve quality. The CVD process is known to produce CNTs of a lower quality than the arc-discharge method [22].

The third widely accepted method for CNT synthesis is called laser ablation which uses lasers to vaporize a carbon source [33, 34] to produce high quality tubes at a temperature of approximately 1200–1500 °C, however the method has reportedly been more expensive than the other two methods to date.

Apart from different methods of manufacturing, the CNTs can also be treated post-production, for example by thermal annealing, which could be used to improve crystallinity and decrease the amount of defects [35], as well as improving interface properties such as electrical contact resistance [36]. Another method of changing or improving the properties of CNTs is called functionalization [32], which is often done chemically by treating the tubes with acids, for instance altering the hybridization from sp^2 to sp^3 in the walls or at the end cap of the CNTs [37]. These methods can change the behavior of the tubes quite significantly, and is further reason to suspect large differences both between methods and within them.

2.1.3 Applications

As of the writing of this text, tens of thousands of metric tons of carbon nanotubes are already being produced each year and their market value is measured in billions of US dollars [31], which is expected to more than double within the next five years according to various market reports. Needless to say, there are already plenty of real world applications for this material, with realistic promises for more and better.

To name a few examples, CNTs have been used as composite materials [38, 39], strengthening mechanical properties [40, 41] or enhancing electrical [42,

43]. They can be used to help store electrical energy, for instance by making good electrodes for supercapacitors, consisting of carbon nanofiber mats covered with CVD grown tubes [44, 45]. There are optical applications such as potentially using CNTs for biomedical imaging and sensors [46], and they have shown promise to be useful for water treatment and desalination of sea water to produce drinkable water at low costs [47]. There is an obvious use for them as electrical interconnects [48], due to their very low electrical resistance and ability to hold high current densities, as well as their small size.

Although the main focus of this dissertation is on the fundamental research of the intrinsic properties, it is always well worth keeping in mind the many practical applications that CNTs already have and what may be realized in the future. To achieve this as effectively as possible however, it is of highest importance the fundamental properties and their sensitivity to material quality are mapped and classified. The work described here hopes to contribute with a small piece of the puzzle to this gigantic task.

2.1.4 Determination of nanotube crystallinity

The aforementioned classification of CNTs requires a careful mapping of the span of crystallinity one should expect for different means of production, and the exact effect on the physical properties that small changes in quality may lead to. Several methods of characterization have been tried in the past, however with a wide spread in results between them, demonstrating the need for standardized characterization methods and material standards for commercially produced carbon nanotube materials. For graphite, as an example, there are well accepted methods to determine material quality, such as Raman spectroscopy and XRD, quantifying interlayer spacing d_{002} and crystallite sizes, both in-plane L_a and across layers L_c, and levels of graphitization [49]. These techniques are also used, together with transmission electron microscopy, to characterize carbon nanotubes, but there are some problems and limitations which will be discussed below.

In Raman spectroscopy the intensity of the D-peak, associated with defects and disorder, is compared to that of the G-peak, corresponding to graphite excita-

tion. Their ratio, $R = I_D/I_G$, is inversely proportional to the in-plane crystallite size L_a [50, 51]. The ratio unfortunately does not depend on defect concentration monotonously, as illustrated for graphene [52], and is also dependent on the excitation wavelength [53]. For tubes, as compared to flat crystals, the intensity of the D-line is also influenced by the curvature of the walls, and not only associated with disorder within the walls [54]. It has therefore been suggested that the R-ratio can only be used as a qualitative measure of the defect density in highly defective tubes [55], and for crystallite sizes below 10 nm [56]. For smaller crystallite sizes, between about 2–10 nm, the width of the G-peak can also be used to directly calculate the in-plane crystallite size L_a, using an empirically derived equation [57]. There were many advances in the field in the last 20 years, and many of the problems facing the technique may be solved in the future, as there are reportedly already great benefits of using the technique on CNTs [58].

In XRD the width of the diffracted peaks corresponding to both in-plane and interlayer spacing can be measured to obtain information on L_a and L_c respectively. As with Raman, the curvature of the tube walls will however influence the results, here affecting the in-plane peaks, which will have long tails towards higher diffraction angles [59]. This effect severely limits the ability to access the in-plane lattice properties, such as L_a, when using XRD or any other diffraction analysis that involves a random distribution of tube orientations.

Analysis using a transmission electron microscope (TEM) is a third approach. Using the actual images of CNT can of course provide a qualitative measure of crystallinity and quality, simply by looking at the tubes using TEM imaging mode. There have been some attempts of turning this information into quantitative data, by using Fourier transforms to quantify the straightness of the walls [60], but very few studies have addressed the crystallinity within the tube walls [61], and analysis has only been possible after substantial image treatment [62]. TEM diffraction has also been used using traditional analysis of peak widths in the radial direction [63], very similar to XRD analysis, but which then have the same problems with spot streaking due to tube curvature.

2.1.5 Methods for electrical characterization

As with methods for crystallinity determination, there are several different techniques to determine electrical conductivity. Different methods report very different results however, and even using the same technique on the same materials, the spread in results is sometimes large and largely unaccounted for. One method involves putting carbon nanotubes randomly on prepatterned electrodes, and measuring those tubes that would by chance bridge the electrodes. Initially the main problem was a very high contact resistance however, in the megaohm range [64], but with some techniques similar to "spot-welding" the contact resistance could be lowered significantly, without doing damage or altering the tubes [17, 64].

One can also use e-beam lithography to lay down electrodes on top of the tubes, a method where one study found contact resistances in the range 0.1–20 kΩ, although the contacts were found to deteriorate after a few weeks of storage [65]. Other studies using two-point measurements found a total resistance in the range of 5–30 kΩ [66]. Using the same technique, it is also possible to have up to 11 electrodes [14], which enables elimination of contact resistance, and led to reported values in the ranges of 6–25 kΩ/µm [14] and 0.2–86 kΩ/µm [16]. Other measurements, including estimates of band gaps, display similarly large spread is the data [67]. None of these techniques had the ability to directly assess the crystallinity or quality of the tubes measured, or to accurately determine the tube diameter and number of tube walls.

In scanning electron microscopes (SEMs) there have been attempts to quantify linear resistance using movable probe setups. The limited vacuum conditions commonly seen in SEMs will however give unwanted electron beam induced depositions (EBID) [36], where any surface exposed by the electron beam during imaging will be covered by an amorphous carbon layer. The effect can be mitigated if the tubes are heated via Joule heating [68]. The SEM images also lack other information, such as information about crystallinity or the number of tube walls that would be available from a TEM analysis.

The method of dipping a CNT into a liquid metal such as mercury has also been examined. The tubes would be fixed at one electrode and the surface

13

of the liquid metal would serve as the other. Then the tube was slowly submerged into the metal, effectively bringing the electrodes closer together. The experiments showed almost no dependence between dipping length and resistance, with the conclusion that the nanotubes are quantum conductors over several micrometers even at room temperature [69]. Unexpectedly however, similar results were shown for several different materials [70, 71], and even for lower quality CNTs made in CVD processes [72]. A serious flaw in the method was later revealed, showing that the nanotubes may not actually penetrate the mercury liquid, but instead the surface of the mercury is deformed [73, 74, 75], like how the mat of a trampoline will deform inwards when a person is standing in the middle of it.

In a TEM, two-point (or many-point) measurements can be done, much in the same way as attempted in the SEM, but with better vacuum which reduces the risk of EBID greatly. The TEM also offers better image resolution, bringing an advantage over SEM studies. Furthermore, this technique can also be combined with the developed methods for determinating crystallinity introduced above. Joule heating can also be used to remove contamination of the tube surfaces, at low enough currents in order to avoid thermal modifications to the tubes themselves [76, 77]. For these reasons, this was the method used throughout the electrical characterizations in this dissertation, and more details on the experimental technique and models of analysis can be found in sections 4.3 and 5.2 respectively.

Chapter 3
Experimental setup

3.1 Samples and preparation

Three different sources of CNTs were used, two from a commercial source (Nanocyl) with CVD grown tubes and a third source with tubes produced by the arc-discharge method. From Nanocyl there were two different grades, the NC2100 and the NC2101. These tubes were marketed as double-walled, purified to greater than 90% carbon, and the NC2101 grade is also functionalised with a carboxyl group (COOH) to reduce bundling. No substantial differences between the two grades were found, so in this work the data is treated as being from the same material. The arc-discharge grown tubes were obtained from Professor Hui-Ming Cheng at the Institute of Metal Research, Chinese Academy of Sciences, Shenyang, China.

The samples were prepared by dissolving the bulk powder in dichloroethane with sonication, or by simply scraping off and/or crushing the sample particles into the finest powder possible. The two methods of preparation had similar results, and the latter one was preferred to minimize the risk of damage, accidental doping or contamination from solvent or sonication [78, 79, 80].

When only measuring crystallinity, a small amount of the nanotube powders were placed on TEM grids (Quantifoil® R 2/1, holey carbon support film), and inserted into the specimen holder. For sessions of both electrical characterization and crystallinity measurement, a small part of the prepared sample was spread out onto a glass surface. A thin silver wire of diameter 0.25 mm was cut to have a sharp edge (about 45°) and dipped into electrically conductive silver epoxy. The edge of the wire covered with epoxy was lowered towards the glass containing the sample while observed with an optical microscope, coming in towards a specimen particle from the side, until the particle was

glued to the wire, as shown in figure 3.1. The particles contained clusters of CNTs. Contact was made using minimal force to ensure the specimen was not embedded in glue, preventing access to protruding CNTs.
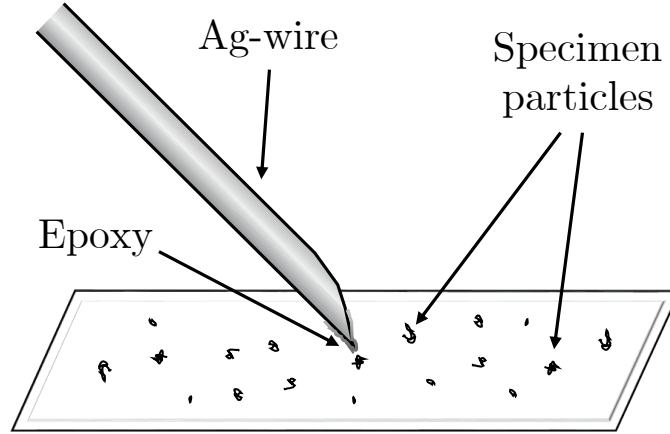
Figure 3.1: Schematic of sample preparation. The edge of the wire covered with epoxy was lowered towards the glass containing particles from the sample, coming in towards a specimen particle from the side, until the particle was glued to the wire.

For electrical characterization, the arc-discharge grown tubes were used exclusively.

3.2   Experimental equipment and calibration

3.2.1   Transmission electron microscope

The main instrument used for the experiments described in this dissertation was a TEM, and a full description of this instrument can be found in the book "Transmission Electron Microscopy" by Williams and Carter [81]. As the name subtly suggests, a TEM is a microscope which uses electrons (as opposed to a "normal" optical microscope which uses light, i.e. photons) to form an image of a sample specimen. Electrons are extracted from a filament and accelerated by applying a high voltage towards the specimen in the part of the TEM called the electron gun. A series of magnetic lenses and apertures are used to control this electron beam, with the intention to make all electrons travel parallel to each other. The electron beam hits the specimen, going through it, making

some of the electrons scatter. The electrons coming out on the other side now contain information about the specimen stored in their trajectories. See figure 3.2 for a schematic of a TEM and the electron beam path.
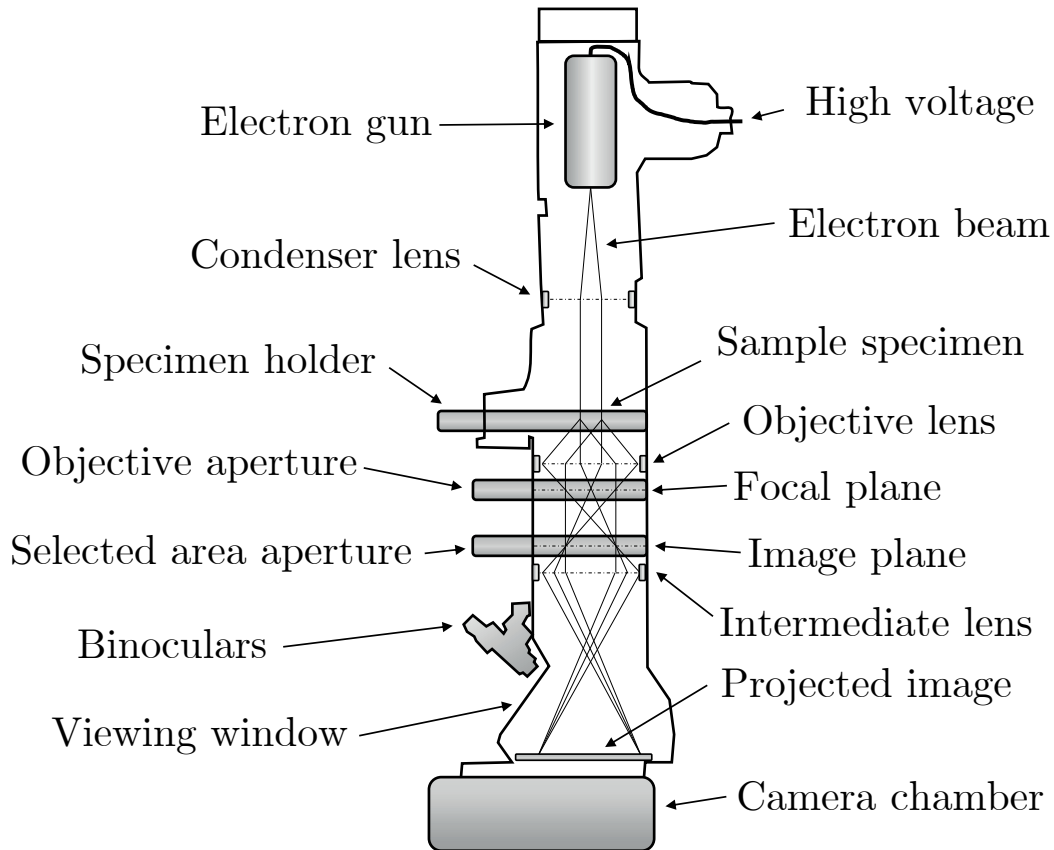
Figure 3.2: Schematic of a TEM. The imaging systems and beam paths are highly simplified, as most TEM have more lenses and apertures.

Following the beam path past the specimen, another series of electromagnetic lenses work together to collect this information and present it to the TEM operator. These latter objective lenses are used to form a focal plane and an image plane of the scattered electrons, and finally to magnify and project an image onto a fluorescent screen or a camera detector, where the focused rays of electrons prepared by the objective lenses can be detected and converted into a viewable image.

By controlling the intermediate lenses the operator of the TEM can choose to

project either the focal plane or the image plane onto the screen. The focal plane is where all rays scattered with the same angle converge at the same point creating what is called a "diffraction image" of the specimen. Conversely, the image plane is the point in space where electron rays originating from the same point in the specimen converge, thus creating a "real image" of the specimen. Furthermore, by inserting an aperture in the image plane, a so called "selected area aperture", it is also possible to select a specific region of the specimen. If one instead inserts an aperture in the focal plane one can remove electrons scattered with a larger angle to improve diffraction focus, or to single out a certain diffracted angle for imaging to create a so called "dark field" image of the specimen. It is also possible to single out only the "central beam" in the focal plane, creating a "bright field" image. The wide selection of operating modes in a TEM makes it extremely versatile when it comes to extracting information about the specimen from the scattered electrons.

Beam-specimen interaction and acceleration voltage

A TEM can be operated at a large range of accelerating voltages, normally between about 100–300 kV but can also be higher or lower. The accelerating voltage determines the speed and energy of the electrons in the beam, which in turn determines scattering angles and influences the resolution of the final image. However, there is also a risk of damaging the carbon nanostructure of graphene or CNT by inducing so called "knock-on" damage, where scattering electrons transmit too much energy to a carbon atom, knocking it out of position or removing it completely. This is of course very undesirable when studying the properties of such structures; we want to avoid changing the sample specimen when studying it. A threshold at 85 kV was reported for knock-on to occur in graphene [82], and already at 100 kV the sample material was found to be altered by the electron beam. Similar conclusions have also been made for CNT elsewhere [83]. In the experiments leading to this dissertation, an accelerating voltage of 90 kV was predominantly used, as this was found to be a balanced option offering slightly more contrast in the resulting images than for 80 kV, while significantly reducing the risk for knock-on damage seen at 100 kV.

Besides keeping voltage moderately low, great care was also taken to direct the beam away from the specimen when not directly imaging, such as when doing other types of measurements or in between image captures. This not only lessens the chance of knock-on damage, but also reduces the build-up of amorphous carbon around the specimen, which can form when hydrocarbons from the background atmosphere stuck to the specimen's surface interact with the electrons coming from the electron beam [84, 85]. The better the vacuum in the sample specimen chamber, the less of a problem this is, something that was made clear when trying a similar experiment inside the significantly worse vacuum of a SEM, see Chapter 3.2.3 for more information on this.

Scale calibration

For calibrations of the scale in the diffraction pattern and estimates of the intrinsic angular spread in the TEM beam, oriented single-crystal gold foils obtained from Electron Microscopy Sciences (EMS Catalog #80038) with lattice plane distances of 0.102 nm, 0.204 nm and 0.143 nm were used.

Specific instrument information

The measurements described in this dissertation were performed at room temperature using a JEOL (JEM 2100) transmission electron microscope equipped with a LaB_6 cathode and a digital camera from Gatan (SC1000 Orius). The main column is pumped with a turbo pump and with the anti-contamination device cooled with liquid nitrogen, the base pressure was around 7×10^{-8} mbar.

3.2.2   Scanning tunneling microscope probe

For electrical measurements, a special custom made specimen holder was used in the TEM. The holder was fitted with a scanning tunnelling microscope (STM) with a compact, three-dimensional, inertial slider design [86], mounted with a tip to be used as an electrode, which could be moved during regular TEM operation. The probe also has the ability to apply a varying voltage bias while measuring the electrical current in a time series.

Several different choices of electrode tip material were tested, where the objective was to obtain a stiff and thin shaped tip with a relatively low and reproducible contact resistance [87]. A commercially available tungsten tip from NaugaNeedles™ coated with platinum (NN-WNP-Pt) as well as a gold wire were both tested. The thin gold wire of diameter 0.25 mm was cut to a sharp edge, and had a reliable and low contact resistance. However, the gold was easily deformed, and proved difficult to cut sharp enough. The coated tungsten tip however was found to have a very reliable and sharp shape, and a high bending stiffness, with a low and reliable contact resistance, and was therefore used for all electrical characterizations. A schematic of the STM experimental setup can be seen in figure 3.3.
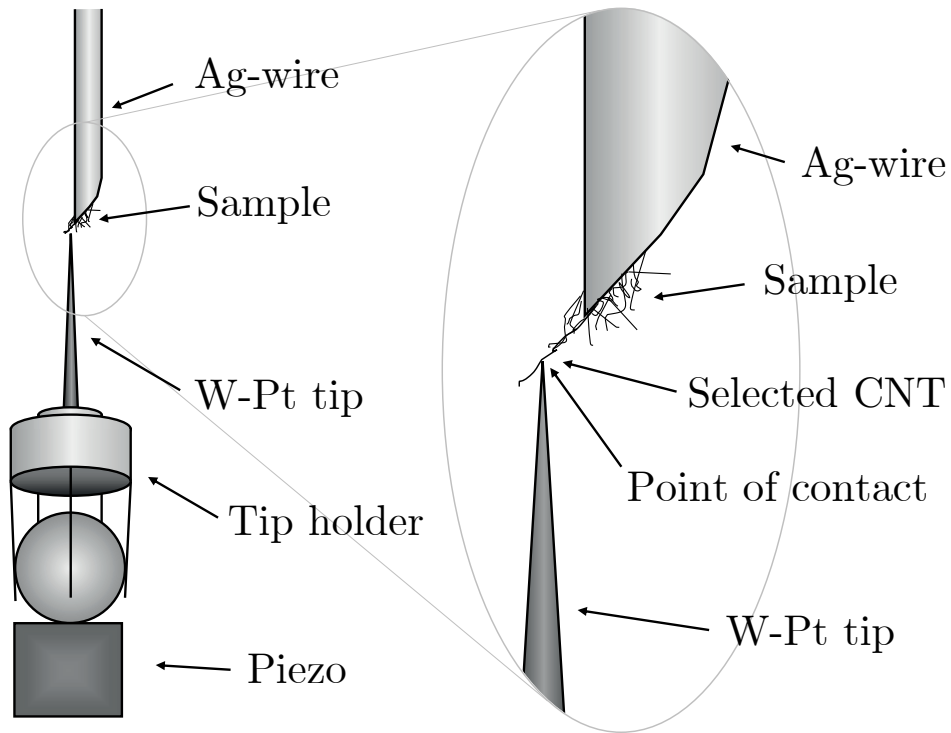

Figure 3.3: Schematic of the electrical probing setup. The sample which contains CNTs is glued to a silver wire. The platinum coated tungsten tip is brought close to the sample by controlling the piezo. The tip makes contact with a selected CNT, enabling the characterization of electrical properties, at several different points of contact along the tubes length.

3.2.3 Scanning electron microscope

All measurements described in this dissertation were made inside a TEM, but it should be noted that before the final experimental setup was decided upon, an alternative setup inside a SEM was also attempted. SEM is the most widely used type of electron microscope. The image is formed by a focused electron beam that scans over the surface area of a specimen, and not formed by instantaneous illumination of a whole field as with the TEM. A full description of the SEM technology can be found for example in the book "Materials Characterization: Introduction to Microscopic and Spectroscopic Methods" by Yang Leng [88].

The attempts were however not successful, as beam-induced build-up of amorphous carbon deteriorated the electrical contacts too quickly, making measurements unstable or impossible. This was likely because of the higher pressure vacuum in this particular SEM of about 5×10^{-7} mbar compared to the significantly lower pressure of the resident TEM of about 7×10^{-8} mbar.

Furthermore, in the SEM there is no possibility to quantify the crystallinity of CNTs. For these reasons the SEM experiments were abandoned in favor of the TEM experiments described in detail in this dissertation. With a lower pressure SEM, however, it should be perfectly possible to conduct the electrical measurements in a similar way as in the TEM, while losing the ability to determine tube crystallinity within the same session.

Chapter 4

Measurements and methods

4.1 Transmission electron microscopy

4.1.1 TEM imaging mode

Imaging mode was used to locate CNTs suitable for measuring, as well as assessing the general quality and state of a sample specimen. As an example, figure 4.1 shows a zoomed out image of a sample with CNTs protruding from the main sample.

Figure 4.1: An example of a TEM image with several CNTs protruding from the main sample, in this case grown by arc-discharge. A platinum covered tungsten tip from the STM probe used for electrical measurements is also shown on the right hand side of the image.

Once a candidate CNT was selected, a closer zoomed image was used for example to select an area for taking diffraction images, or (as shown in figure 4.2) for making contact with the STM probe tip in order to make electrical

measurements or otherwise manipulate the specimen.

Figure 4.2: An example of a TEM image where the STM probe tip is making direct contact with the nanotube.

It is also perfectly possible to assess many properties of CNTs visually, in image mode. This can many times be done quantitatively and with great precision for such properties as nanotube inner and outer diameters, the number of tube walls etc. However, for some properties like for example crystallinity or rates of defects within the CNT walls, average distance between MWCNT walls, or chirality, it may be hard or impossible to obtain quantitative measurements, and such properties can often only be assessed qualitatively. In figure 4.3 for example one can see qualitatively the difference in crystallite size and quality between (a) CVD-grown CNTs and (b) CNTs grown by arc-discharge.

4.1.2   TEM diffraction mode

As established in the previous section, some properties can be qualitatively assessed in imaging mode, but it may not be easy to obtain quantitative information. Some of these properties are better analyzed by using the TEM diffraction mode.

In diffraction mode, as briefly touched upon in section 3.2, we get a picture of all the scattering angles of the electron beam, instead of a picture of the actual sample specimen. A full description of diffraction theory is of course beyond
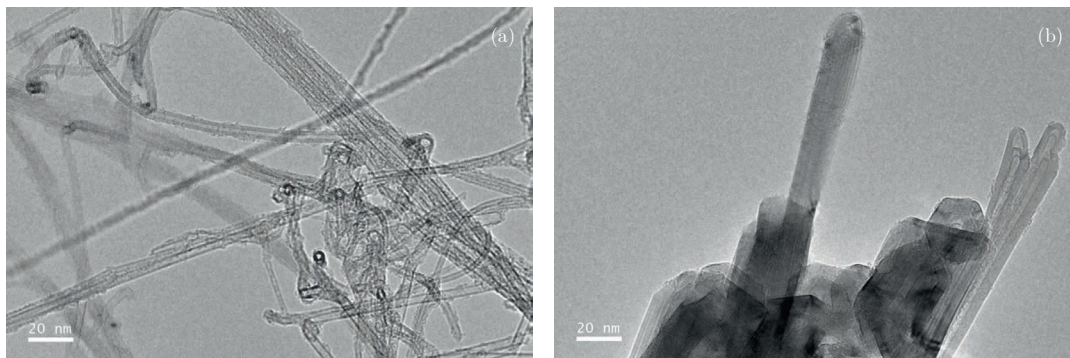
Figure 4.3: TEM images of (a) CVD-grown CNTs and (b) AD-grown CNTs. Here, one can qualitatively see the difference in crystallite size and quality between the two production methods.

the scope of this dissertation, but can be found in the book "Transmission Electron Microscopy" by Williams and Carter [81]. In a much simplified view, the electrons will scatter in the same angle when passing through gaps of the same size. These gaps in the specimen basically corresponds to distances between atoms, or rows of atoms, which is why diffraction is such a powerful tool when studying atomic structures even when using microscopes whose resolution is not high enough to resolve individual atoms, as is the case with the TEM used here.

The specific mode of TEM diffraction used here is called selected area electron diffraction (SAED). By inserting an aperture in the image plane, the "selected area aperture", we can select for a specific part of the image, which makes it possible to isolate a section of a single CNT to contribute to the diffraction image. A more detailed description on how such an image can be analyzed can be found in section 5.1.1, where an example of a SAED image where a section of a CNT has been selected can be seen in figure 5.2.

4.2 Measuring carbon nanotube crystallinity

4.2.1 Tube selection

The selection of an appropriate CNT for crystallinity measurement has an unavoidable selection bias, which is related to the diameter of the selected area

aperture. Only a straight section of the tube with a length at least equal to the diameter of the aperture was eligible for measurement. Furthermore, the space in the direction perpendicular to the section's length should be mostly empty, in order to minimize interfering diffraction from other sources than the tube in question. For measurements described here a selected area aperture of diameter 105 nm was used. Measured samples are thus biased towards freely hanging tubes with straight sections of at least 105 nm, and against tubes that are bundled together.

4.2.2 Measurement

Once the section of a tube was chosen, the selected area aperture was inserted and placed appropriately, masking everything but the section of tube to be measured. The TEM was switched into diffraction mode, and the camera distance was set to 40 cm. The blanker was placed over the central spot to avoid damaging the camera. The brightness, corresponding to TEM beam diameter, was set to the predetermined value appropriate for crystallinity measurement, and the diffraction focus setting was taken from the corresponding value for optimal focus. The predetermination of the proper settings was done with a calibration sample, described in more detail in section 5.1.3. A series of measurements with different brightness settings was done for each tube to increase accuracy. Images were taken over a duration of about 30–60 seconds, to obtain a sufficient intensity without over-saturating any points of the image. The duration of the image capture only has an influence of the height of the diffraction peaks, but not on the shape and breadth, which makes measurements insensitive to differences in this setting. The analysis of the resulting images is described in section 5.1.1.

4.3 Electrical probing

4.3.1 Tube selection

Analogous to the selection of tubes described in section 4.2.1, there is an unavoidable selection bias for the electrical measurements. In order for electrical probing to be possible the tube needs to be protruding from the rest of the sample sufficiently, at least a few hundred nanometers, and in a direction at least $\theta = 30°$ perpendicular to the incoming tip, or more. The reason for this is geometrical, so the tip is cleanly able to make contact with the tube at several points without touching other tubes, as shown in figure 4.4.
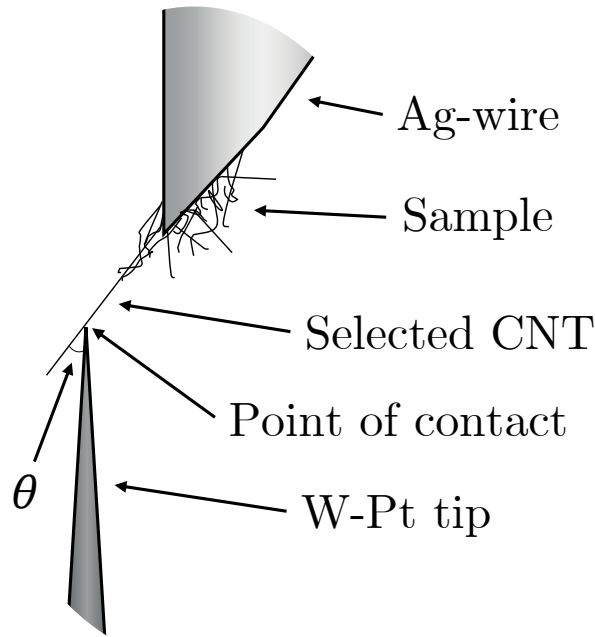
Figure 4.4: A schematic of the experiment showing the silver wire holding the sample specimen, and the platinum coated tungsten probe tip, as the tip makes contact with a CNT.

The tip was moved close to the tube with coarse piezo movements, and finally brought close enough to make contact by using fine piezo movement. Once the tip was close enough to the tube, the tube commonly "snapped" to the tip, due to van der Waals forces. To avoid possible mechanical strain that could be exerted upon the tube by the tip, the tube was returned to its free hanging

position by moving the probe tip along with the tube.

End-contact between the tip and the CNT was avoided since this is known to have a significantly lower contact resistance than side-contact [87, 89, 90]. This is due to the stronger atomic bonding at the tube's end, compared to van der Waals bonding on the tube's side. Furthermore, end-contact may also increase the probability of accidentally connecting the electrode to multiple tube walls [91], which would unintentionally increase the number of conducting channels, distorting the results.

4.3.2 Contact resistance and annealing

During electrical characterization, the electron beam from the TEM was directed away from the sample and tip to prevent beam-induced damage and amorphous carbon deposition. Contact resistance was found to be generally relatively high and unstable. To mediate this, a process of electrical annealing was implemented by way of Joule heating [36], which generates heat by applying a current. The power of the heat generated is proportional to the current times the bias voltage, or

$$P_{\text{heat}} \propto IU. \tag{4.1}$$

The generated heat anneals the tip to the sample, reducing, stabilizing and standardizing the contact resistance. To ensure there was no damage to the tube or tip, the annealing current was kept under 100 µA which in this case meant applying a voltage bias of 2 V.

The threshold of approximately 100 µA was found by trial-and-error, and applies to this specific experimental setup and choice of samples. Increasing the heating power beyond this point often resulted in catastrophic failure of the tube. The point of failure where the tube burns off is approximately in the middle of the tube protrusion, equally distanced from the point of contact and where the tube touches the base sample. To ensure that the tube was not damaged even when keeping the current lower than this, a number of tests were made by measuring the CNT crystallinity by using the diffrac-

tion method explained above, before and after annealing, which showed no significant differences between measurements.

The anneal was divided into three phases; increase, hold and decrease, where bias was increased linearly to 2 V during 2 seconds, held for 10 seconds, and finally reduced back to 0 V during 2 seconds. An example of this process can be seen in figure 4.5.
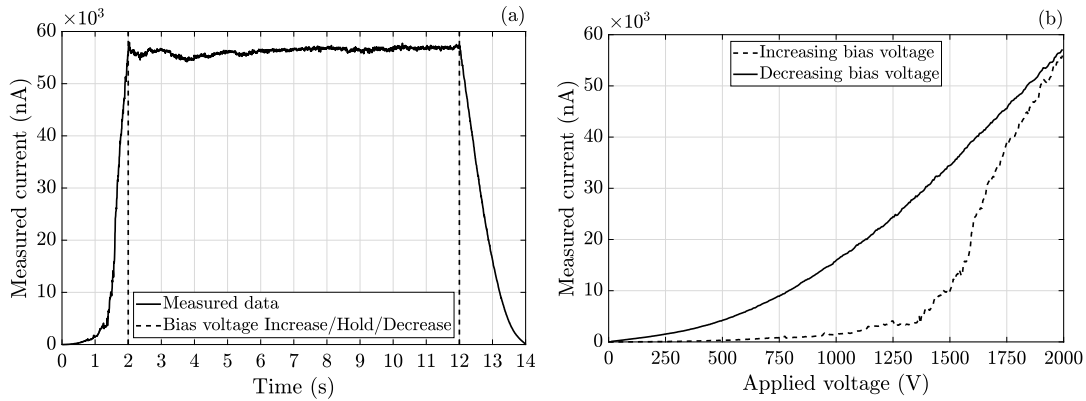
Figure 4.5: (a) Current plotted versus time for a typical anneal, where the bias was increased linearly to 2 *V during* 2 *seconds, held for* 10 *seconds, and finally reduced back to* 0 *V during* 2 *seconds. (b) Current versus applied bias voltage for the same example, with both increasing and decreasing bias.*

After the increase phase and the first two seconds of the hold phase of the anneal, the contact resistance was found to be relatively low and stable. However, for each new point of contact annealing had to be repeated in order to maintain stability and accuracy of the following measurements. This also meant that there was a risk of continually lowering the tip/tube contact resistance for each measurement made. Through thorough testing by making several passes along the tube, starting from closest to the sample and going out, and then inwards again, measuring at several points along the way, this possible source of error could be disregarded, as no discernible differences in the contact resistance were found. The variability of the contact resistance after annealing is discussed further in section 5.2.2.

4.3.3 Measuring electrical resistance at a point of contact

As can be seen in figure 4.5 (b), the current/voltage relationship becomes superlinear at higher bias voltages. This is due to the tunneling currents between the walls of the MWCNT [14, 92]. Such "intershell" conduction is of course a very interesting property for a multi-walled nanotube, however in this work the objective was to connect conductivity with the crystallinity of the outermost wall. Thus, to ensure outermost wall conduction was the dominating mode of electron transport, the bias voltage was kept below 5 mV for measurements of point resistance, as is shown in the example in figure 4.6. The resistance was found to be ohmic at low bias after annealing, and the mean value of the differential resistance in these measurements corresponds to the average measured resistance R_p of the point of contact.
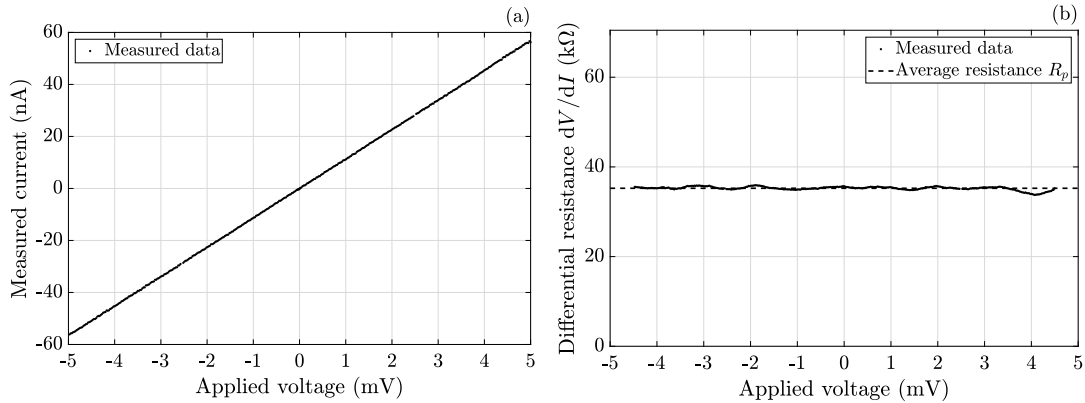
Figure 4.6: *(a) Example of an I-V plot from one point of contact. Bias voltage was varied from −5 to +5 mV. When measuring, the bias is kept sufficiently low to maintain and ohmic (linear) relationship between the current and voltage. (b) The corresponding dV/dI plot, and a fitted line corresponding to the average measured resistance of the point of contact.*

After measuring the electrical resistance of a point, the distance between electrodes l_p was measured using TEM imaging for each point of contact. For the position of the electrode on one side, the point of probe/tube contact was used, shown as point 1 in figure 4.7. On the other side the tube's closest contact with the silver wire, conducting glue or other part of the sample in contact with the wire was used. The actual wire/tube contact was often obscured, in

30

which case the point where the tube is no longer visibly free hanging was used, shown as point 2 in figure 4.7.
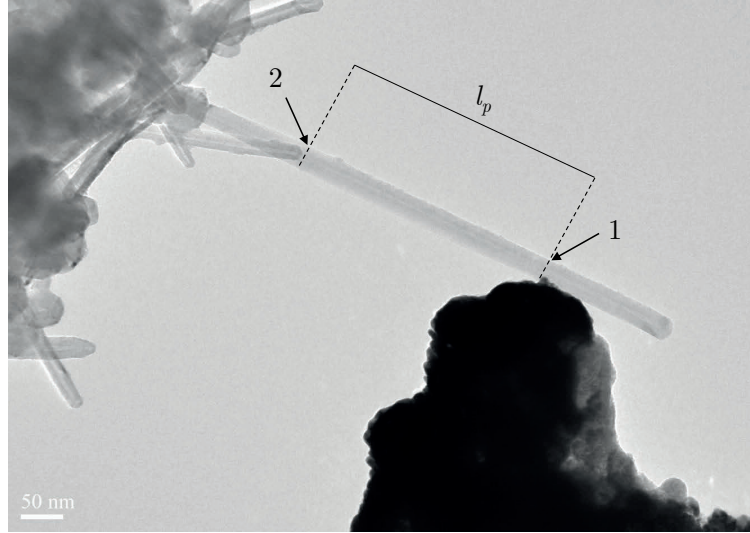
Figure 4.7: A TEM image picturing an example of a point measurement. The distance l_p was measured between point 1 where the probe tip is in contact with the tube, and point 2 where the tube is no longer visibly free hanging.

After one cycle of point measurements, as was described above, the tip was slowly retracted from the tube wall until contact was broken. The sequence was repeated for each tube until a sufficiently large set of measurements was obtained, taking into account the number of contact points, the range of l_p and the variance of each point measurement.

Chapter 5
Analysis and modeling

5.1 Crystallinity

5.1.1 Analysis of a carbon nanotube diffraction pattern

In the description of the TEM in section 3.2, we learned that the intermediate lens of the microscope can be altered so that the focal plane is projected onto the viewing screen instead of the image plane. This produces a diffraction image. The theory of diffraction was initially developed for light, i.e. photons and electromagnetic radiation waves and wavelengths, but works equally well for matter waves with de Broglie wavelengths. The energy used to accelerate the electrons in the TEM requires relativistic correction to the formulas, so the wavelength of the electrons involved can be calculated by

$$\lambda = \frac{h}{p} = \frac{h}{\sqrt{2m_0 eU + \left(\frac{eU}{c}\right)^2}},$$ (5.1)

where the acceleration voltage of the TEM electron gun is denoted U, and where h, m_0, e and c are Planck's constant, the rest mass of an electron, the charge of an electron and the speed of light respectively. The acceleration voltage used throughout the experiments described in this dissertation was 90 kV, which gives a wavelength λ of about 3.919 pm.

A detailed description of crystallography and the theory of diffraction is a subject in its own right, and an introduction can be found for example in reference [93]. As a first approach to understanding diffraction images of CNTs however, one can think about the atoms and layers of carbon atoms that make up the CNT as repeating patterns, with repeating distances. We call such a repeating pattern a "lattice" and the distance between subsequent repetitions

33

is called a "lattice distance". In a simplified view, the incoming electrons in the TEM beam will diffract to the same angle when passing through lattice distances of the same size. Thus, a specific lattice distance will be projected to a specific distance r from the center of the diffraction image. The azimuth angle of the lattice determines the direction from the center of the diffraction image, and if two lattices have two different angles, then the angle between them will be preserved in the diffraction image. In figure 5.1, a schematic example of this is shown, where the specimen is imagined to have two lattices with different lattice distances, whose azimuth angles also differ by $\delta\psi$, which is preserved in the diffraction image. The angle between the incident beam of electrons and the diffracted beam is traditionally called 2θ, and is connected to r by

$$r = D\tan 2\theta, \tag{5.2}$$

where D is the distance between the specimen and the projection screen.
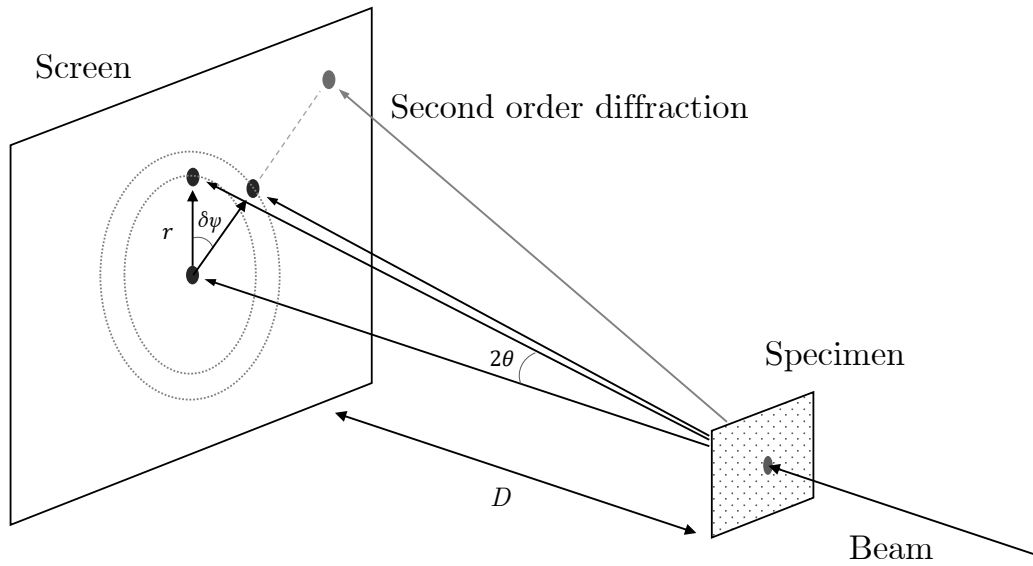
Figure 5.1: Schematic of a diffracted beam of electrons. D is the distance between specimen and screen, 2θ is the radial diffraction angle, $\delta\psi$ is the angle between two differently spaced and angled lattices in the specimen, and r is the distance between the central spot on the screen to one of the corresponding diffraction spots. The image also shows both the first and second order diffraction spots for the other diffracted angle.

To better understand how the diffraction image corresponds to the specimen

lattice, we can consider a few short examples. If a certain lattice distance and angle occurs frequently enough in the sample specimen, a well defined spot will appear in the diffraction image. If instead the specimen contains a certain lattice distance but where all angles occurs randomly with an even distribution, as for example if the specimen is a powder of randomly oriented crystals, a ring shaped pattern will be seen in the diffraction image. Conversely, if the specimen contains a span of different lattice distances all oriented in the same direction, a diffraction spot will be stretched out into a line segment.

The connection between lattice distance d and the diffraction angle 2θ described above is formulated mathematically by the well known physics formula Bragg's law, usually stated as

$$n\lambda = 2d \sin\theta, \tag{5.3}$$

where λ is the wavelength of the diffracted wave (in our case the beam of electrons). In 5.3 we also see the symbol n representing the "order of diffraction", which is an arbitrary integer. What this says is that by following the line from the center of the diffraction image to the diffraction spot, and then continuing outwards, we will find more spots that are "of higher order". Furthermore, since the integer n can be both positive and negative, we will also find spots diametrically across the center point, with the same distances from the center. Lastly, since n can be zero, it says that all lattice distances and angles will contribute to the spot in the dead center of the image, making this spot very bright. In figure 5.1 a "second order diffraction" spot, which means $n = \pm 2$, is shown as an example.

From Bragg's law we see that the lattice distance d is inversely proportional to the sine of half the diffraction angle 2θ seen in figure 5.1. For illustrative purposes it is useful to exploit the small angles involved in electron diffraction by making the approximations $\sin x \approx \tan x \approx x$, which gives us that $r = 2D\theta$ and $n\lambda = 2d\theta$. Putting these together to eliminate θ results in $r/D = n\lambda/d$ or

$$d = D\lambda \cdot \frac{n}{r}. \tag{5.4}$$

Since the distance between specimen and screen D and the wavelength λ are

presumed to be constant in our measurements, we don't have to know them. Instead, we can calibrate the scale of r in the diffraction image by using a specimen with a pre-known lattice distance such that we get

$$d = \frac{n}{r}. \tag{5.5}$$

Thus, knowing the order of diffraction n, we only need to measure the distance r between the diffraction spot and the center of the image, in order to get the lattice distance d, up to a negligible small angle approximation error.

An example of lattice distance determination

As an example where we can get a good quantitative measurement in both imaging mode and diffraction mode, making it possible to compare the results confirming their validity, we can look at the average distance between the walls of a MWCNT, known to be similar to that of turbostratic graphite, although with a slight dependence on the tube diameter [30]. In figure 5.2 (a), a MWCNT with visible individual walls is shown, where a section of the walls have been selected for a pixel count. In the inset upper right image, one can see ten peaks and valleys in the pixel count inside a distance of about 3.52 nm. This results in a mean wall spacing of about $3.52/10 = 0.352$ nm, for the selected rectangular area of the CNT.

Now consider figure 5.2 (b), showing the diffraction pattern corresponding to the selected area marked by the black mask in figure 5.2 (a). Here, the two spots marked by white arrows indicate the diffracted angles that corresponds to the spacing, or gap, between the CNT walls, sometimes denoted d_{002}, from the similarity with the interlayer distance of Bernal-stacked graphene. Gaps in the atomic structure of the CNT with similar width and angle will all contribute to the brightness within these spots, meaning that the very peaks of the spots will correspond to the most common wall spacing. The distance of these spots from the center of the diffraction image, measured in inverse units of length, is the reciprocal of the wall spacing. Comparing figure 5.2 (a) and (b) we can also see that the spots appear on a line perpendicular to the tube's length, and that there are diffracted spots of the second order on the same line but farther
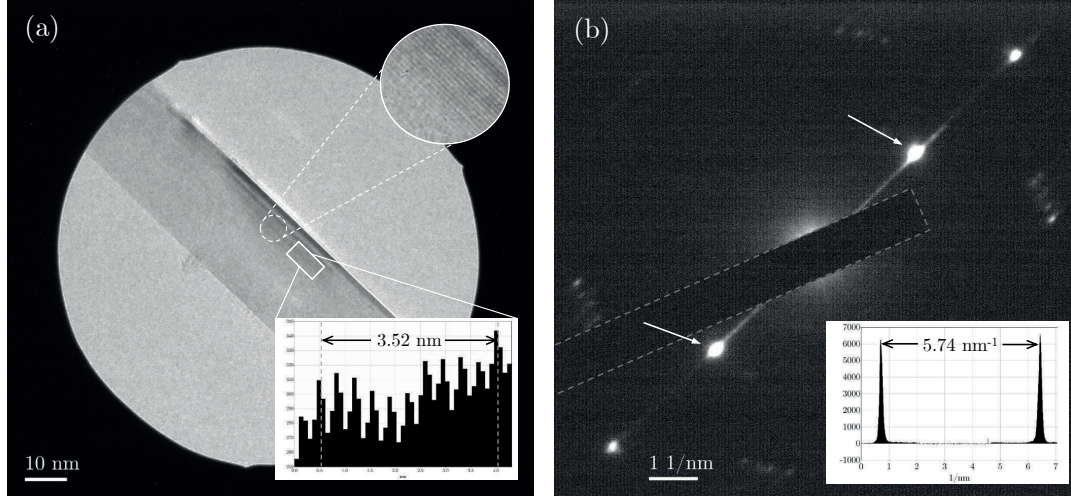
from the center.

Figure 5.2: (a) A TEM image of a MWCNT, where individual walls can be seen. The black mask seen surrounding the CNT is the selected area aperture. Inset upper right: A circular area of the tube is zoomed in, showing the tube walls. The white rectangle indicates the area of individual walls selected for a pixel count. Inset lower right: A pixel count of the white rectangle area taken perpendicular to the tube axis, where ten peaks and valleys are selected for measuring, thus giving a mean wall distance. (b) A diffraction image of the selected area marked by the black mask in figure (a). The central beam spot is covered by a mechanical blanker inside the TEM, since the brightness of this spot would damage the camera. The two arrows point to the two symmetric spots corresponding to the CNT wall distance. Inset lower right: A pixel count following the line defined by the two marked diffraction spots in figure (b).

In the inset lower right of 5.2 (b), the distance between spots is measured to be 5.74 nm^{-1}, so the distance from center is approximately 2.87 nm^{-1}. The reciprocal of this is $1/2.87 \approx 0.348$ nm which is slightly smaller than the result from the imaging mode analysis. It is worth noting that the result from diffraction mode analysis takes into account all parts of the CNT which can be seen in figure 5.2 (a), while the former result only takes into account the region within the narrow white rectangle.

The above example illustrates how diffraction mode can be used, in this case to quantify the spacing between tube walls. However, the same technique can also be used to gather information about individual atom spacing within each wall, in all directions where the same spacing is repeated, in the same angle. For instance, the hexagonal lattice formed by carbon atoms within the wall

of a CNT ideally produces a hexagonal pattern around the diffraction image center, and by measuring the distance to these diffraction spots it is possible to calculate the lattice distance and infer information about the orientation of the lattice within the CNT wall.

Tube chirality

Apart from information about lattice spacing and angle, there is more to be found in the diffraction image. Another property of carbon nanotubes is their chirality, the specific way they are "rolled up" into tubes. This has been investigated with SAED in a TEM by, among other things, comparing different tilting angles of the same CNT to the relative position of diffraction spots [94, 95, 96], and also by comparing patterns to simulations to match a certain chirality [97, 98, 99]. Although not pursued in this dissertation, the determination of chirality would be a useful complement to the measurements that are done here, and should be considered in the continuation of this work. The techniques are however not without problems, and in a review article from 2011, Allen et al. finds that "many of the analyses, when used in isolation, are insufficient to ensure unambiguous determination" [100], showing that several different methods of chirality analysis may be needed to uniquely determine tube chirality from TEM diffraction images.

Spot streaking

In a diffraction image produced by using high crystallinity graphene as the target specimen, the diffraction spots corresponding to the hexagonal lattice of carbon atoms would be sharp and well defined. For CNTs however, even though they can be thought of as rolls or cylinders of graphene, one will seemingly get unsharp and smeared spots, as can be seen for example in figure 5.2, in the direction perpendicular to the tube's length. This effect is called "streaking", and stems from the curvature of the tubes; as the "graphene" that makes up the tube wall bends into a cylinder, the apparent lattice distance becomes less well defined, and the width of the specimen becomes limited by the tube's diameter. In the direction of the length of the tube we do not see

any streaking, since in this direction the lattice distances are well defined and constant, and the size of the lattice is not limited by the tube's diameter, only by the tube's length (or the selected area aperture's diameter). Using this information we can clearly see the direction of the tube even in the diffraction image, and it also contains information about the tube's curvature, and thus its circumference. The manner in which the spots display streaking is also an important piece of information when determining tube chirality, as described above. In figure 5.3 an example of diffraction from a multi-walled tungsten disulfide (WS_2) nanotube is shown.
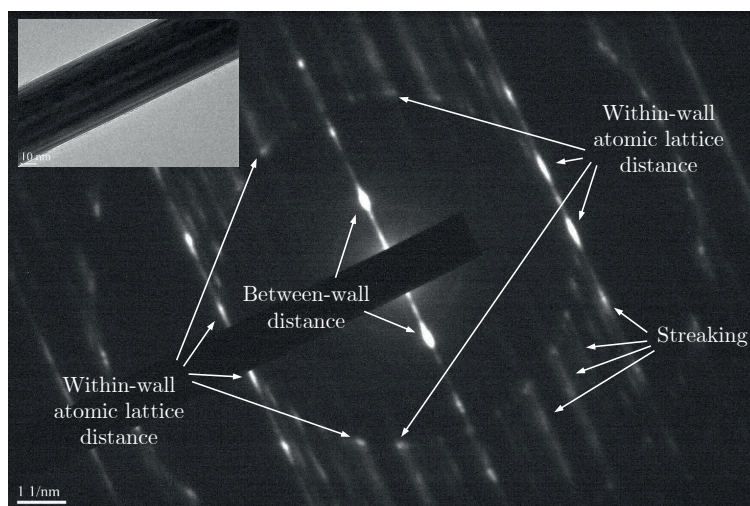
Figure 5.3: An example of diffraction from a multi-walled tungsten disulfide (WS_2) nanotube. Arrows in the image point to the diffraction spots that correspond to the between-wall distance (the innermost spots), and the spots that correspond to some of the within-wall atomic lattice distance. The inset upper left shows the region of tube selected for diffraction.

A tungsten disulfide nanotube has a very similar geometry as a MWCNT, with concentric tubes having a similar circumference, but in general has a higher degree of crystallinity within its walls, and can thus be used to show the effect of streaking more clearly. Several within-wall spots are on an equal distance to the center describing a circle, and besides the between-wall spots there is nothing inside this circle, which implies that the spots correspond to the largest lattice spacing that allows diffraction within the walls. Outside of the circles, spots that correspond to other lattice distances can be found, but here we also see the image being dominated by streaking from the innermost spots, in the

direction perpendicular to the tube's length.

5.1.2 Diffraction spot width and crystallite size

Besides the fact that atomic lattice distances and their relative angles can be identified in the diffraction image, and that the curvature of these lattices is related to streaking diffraction spots, there is also a connection between the total size of the lattice and the sharpness, or width, of the corresponding diffraction spot. The within-wall lattices may span the CNT for many nanometers, but at some point there may be a line of defects, or a border that divides two different orientations of similar hexagonal lattices apart. It is common to call a perfectly ordered region of piece of atoms a "crystal", so in this case we can call each such well ordered region within the same tube "crystallites". A CNT with large crystallites and low rates of defects is said to have "high crystallinity".

For graphite and graphene, the in-plane crystallite size is traditionally denoted L_a, and the same symbol is used for the analogous within-wall crystallite size of CNTs. The across-plane crystallite size of graphite is called L_c, and the same notation is used for the across-wall crystallite size of MWCNTs. An illustration showing the in-plane crystallite size L_a along with the between-wall distance d_{002} and the across-walls crystallite size L_c is shown in figure 5.4.
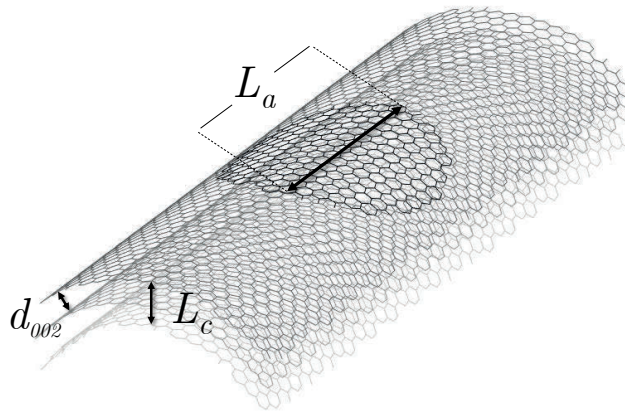

Figure 5.4: Illustration of the crystallite sizes L_a and L_c, and the between-wall distance d_{002}, in the context of a MWCNT with multiple crystallite regions (one such region is highlighted in black).

Deriving an expression for crystallite size

The connection between crystallite size and how wide the diffraction spot becomes can be derived in several ways. In the book "The Basics of Crystallography and Diffraction" by Hammond [101], the dependence is derived using the condition for destructive interference on each side of the peak, connecting the peak width to the crystallite size. The most common expression used in XRD is the equation suggested by Paul Scherrer in 1918 in his paper "Bestimmung der Größe und der inneren Struktur von Kolloidteilchen mittels Röntgenstrahlen" [102], later to be referred to as the "Scherrer equation". In his original paper, the expression is given in a slightly different format, but the commonly used expression is

$$\tau = \frac{K\lambda}{\Delta(2\theta)\cos\theta},$$ (5.6)

where τ is the mean size of the ordered domains, or crystallites as we have called them, λ is the diffracted wavelength, θ is half of the diffraction angle as seen in figure 5.1, $\Delta(2\theta)$ represents the width of the diffraction spot and K is a "correction factor" that corrects for differences in crystal geometry.

The correction factor K is called "the Scherrer constant" or "the shape factor", and depends on the geometrical shape and structure of the crystals. It has been calculated numerous times but with varying results depending on the definition of peak width and several other details. For an excellent review of issues surrounding the constant K and most other aspects of the Scherrer equation, see "Scherrer after sixty years: A survey and some new results in the determination of crystallite size" by Langford and Wilson from 1978 [103]. The overall consensus in the field seems to be that this factor is very close to 1 for most shapes, including cylinders (like a nanotube). To not complicate things unnecessarily and to avoid potentially correcting the wrong way, the value for K used in this dissertation was $K = 1$.

The diffraction spot has a highest intensity somewhere within the spot, and this is called the "peak". Thus the width of the spot is usually called the "peak width", and is also sometimes denoted as β. It is however not completely trivial just how to quantify the width of such a peak. For completely symmetrical

and bell-curve (Gaussian) shaped peaks it makes sense to use the full width at half maximum (FWHM) an the width of the peak, but for other peak shapes the more generally defined "integral breadth" should be used, which is the width of a rectangle with the same height and area as the peak.

As we did with Bragg's law in section 5.1.1, we may simplify the Scherrer equation for our small angle situation to be independent of diffraction wavelength and diffraction angle. To arrive at the small angle approximation of Bragg's law in equation (5.5) we have calibrated the scale of our TEM diffraction images such that $r = 1/d$. Reinserting this into Bragg's law in equation (5.3) we get

$$n\lambda = 2 \cdot \frac{1}{r}\sin\theta, \tag{5.7}$$

or

$$\theta = \arcsin\left(\frac{n\lambda r}{2}\right). \tag{5.8}$$

In Scherrer's equation we have a change in the angle 2θ, and for this angle we have

$$2\theta = 2\arcsin\left(\frac{n\lambda r}{2}\right). \tag{5.9}$$

Thus, for a small change in 2θ called $\Delta(2\theta)$ we get a small change in r, called Δr, described by

$$\Delta(2\theta) = 2 \cdot \left(\arcsin\left[\frac{n\lambda}{2}\left(r + \frac{\Delta r}{2}\right)\right] - \arcsin\left[\frac{n\lambda}{2}\left(r - \frac{\Delta r}{2}\right)\right]\right). \tag{5.10}$$

For small angles we have $\arcsin x \approx x$, so we get

$$\Delta(2\theta) = 2 \cdot \frac{n\lambda}{2} \cdot \left(r + \frac{\Delta r}{2} - r + \frac{\Delta r}{2}\right) = n\lambda\Delta r. \tag{5.11}$$

We also have the small angle approximation of $\cos x \approx 1$, and inserting all this into (5.6) we get

$$\tau = \frac{K\lambda}{n\lambda\Delta r} = \frac{K}{n\Delta r}, \tag{5.12}$$

which is a small angle approximation of the Scherrer equation using the same image scale calibration as before.

In our case we will be measuring the breadth of a single diffraction spot, which

corresponds to the orientation and domain size of one single crystallite in the tube's wall. Recall that Scherrer's equation was written with respect to XRD, where the common practice is to look at a powder of crystals, which means that all angles of orientation are present in the specimen simultaneously, and why τ is the "mean" size of crystallites. Here, τ corresponds to the within-wall crystallite size L_a, and we can drop the word "mean". Using this notation instead of τ, and swapping Δr for the traditionally used β denoting peak integral breadth, we can now write our final expression describing the crystallite size L_a corresponding to the first order diffraction ($n = 1$) peak breadth β, and with the geometrical constant K approximated to 1, as

$$L_a = \frac{1}{\beta}. \tag{5.13}$$

Our two simplified expression (5.5) and (5.13) better illustrate the overall dependencies between crystallite lattice spacing and diffraction spot position compared to crystallite size and diffraction spot width, and it also shows their analogous behavior; smaller lattice spacing produces spots farther from the image center, and smaller crystallites broaden the diffraction spots.

Elimination of streaking

The fact that the width of a diffraction spot can be used to determine the size of the crystallite from which it originates also shows why streaking diffraction spots may be a problem for such measurements. In the direction perpendicular to the tube's length we get streaking spots stemming from the curvature of the tube, making a proper width determination of the peak more difficult. Besides this, the actual size of a crystallite in this direction will be limited by the tube's circumference or less. For these reasons, all measurements for proper determination of L_a should be done in the direction parallel to the tube's length. An example of such a measurement is shown in figure 5.5 (a), where the white rectangle on the bottom right marks the area of an intensity line scan. In figure 5.5 (b) the corresponding line scan data is shown as a peak, and the peak is fitted to a Voigt function. To the left in figure (b) it is possible to see a "bump" in the data due to interference from an adjacent diffraction
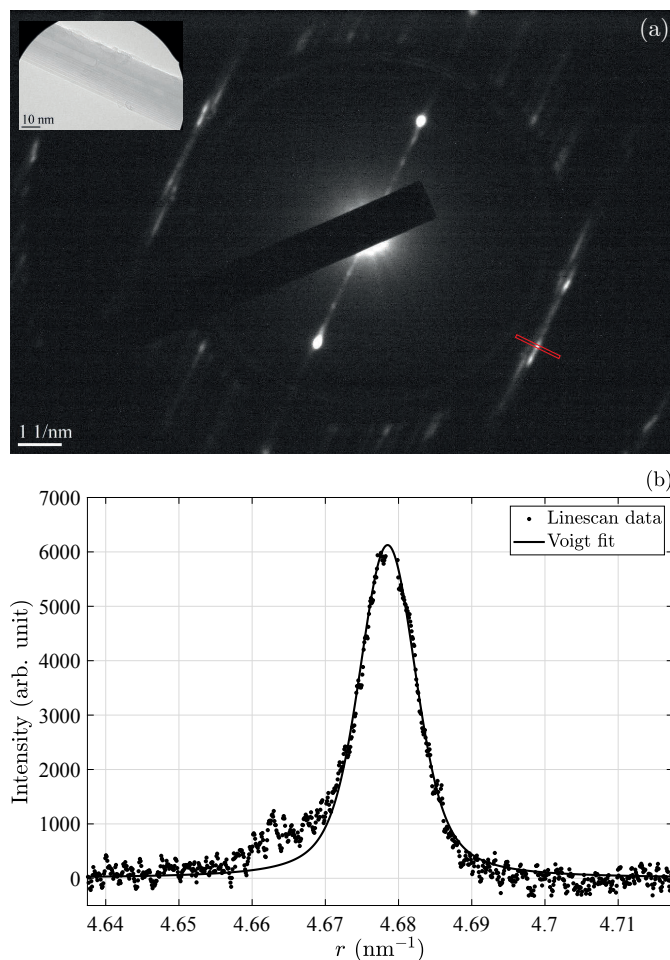
spot's streaking.

Figure 5.5: Example of a line scan made along the tube axis. The narrow rectangle on the bottom right of (a) marks the line scan region. Inset: Selected area aperture showing the CNT. In (b) the corresponding line scan data and a fitted Voigt function, where the x-axis is the distance r from the central spot to the measured spot, in the scale calibrated such that $d = 1/r$, where d is the corresponding lattice distance.

As is apparent from the above description, the exact details around expressions for crystallite size are not completely simple to obtain. There is however no contention involved in the dependencies of crystallite size to peak width. The relative measurements of crystallite sizes are therefore perfectly measurable, even though the exact values of these should be interpreted with a healthy dose of wariness. To make matters even worse, the peaks can also have several other sources of broadening apart from crystallite size, for instance due to the instrument used in measuring or due to strain present in the crystallite, and

in the next section we shall detail these as best we can, and see what can be done to eliminate or minimize these contributions to the overall peak integral breadth.

5.1.3   Deconvolution of the sources of broadening

Apart from the width (or more accurately breadth) and height of a diffraction peaks, they can also differ in shape. To model these shapes, a commonly used probability distribution in spectroscopy is the Voigt profile, which is the convolution of a Gaussian and a Lorentzian distribution.

The final shape and breadth of a diffracted peak can have several different sources, including instrument contributions, strain due to disorder or stress in the atomic lattice structure, and the finiteness of the crystallite size. Thus, if one were to use the full integral breadth of the peak in equation (5.13) the results would represent an lower bound for crystallite size, since we expect its actual contribution to be smaller than the full breadth of the peak. Here the assumption was made that the broadening effect from a crystallite size is purely represented by the Lorentz contribution, and the strain effect is represented by the Gauss contribution, as is common for single-line spectroscopy analysis [24, 104, 105]. The validity of such an assumption depends on several factors, and can be another source of error, however it was found throughout the analyses in this dissertation that the assumption in general is successful and effective in isolating broadening stemming from crystallite size.

The division into a crystallite size part, and a strain part, can however not be done before first subtracting instrument broadening. The instrumental broadening was estimated by using a single-crystal gold sample and selecting a large, homogeneous, area for SAED analysis.

Diffraction spot broadening in TEM diffraction stems mainly from the failure to produce truly parallel beams of electrons with the condenser lenses, as seen in figure 3.2. The slight angle that remains in turn depends of the diameter of the TEM beam spot, which is controlled by the "brightness" setting on the TEM. To quantify this dependence, a series of measurements were made on

the calibration sample with varying beam diameter.

The diffraction image must also be in optimal focus when measuring, and this is usually done by the TEM operator manually, by varying diffraction focus around the optimal focus setting. This optimal setting also depends on beam diameter, so in order to have the correct focus for each beam diameter, a series of focus measurements were taken for different beam diameters. A power function was fitted that relates the optimal focus to the brightness setting, so that in subsequent measurements the correct focus setting could be applied for each beam diameter in a systematic way, instead of relying on manual assessment by the TEM operator.

The measurements made when varying beam diameter were fitted with Voigt profiles, consisting of a Gaussian part and a Lorentzian part. The peak integral breadths are denoted β_V, β_G and β_L for the three profiles respectively. Due to the fact that the convolution of two Voigt functions is again a Voigt function, we can split up each of the two contributing parts into their instrument and sample parts,

$$\beta_L = \beta_L^I + \beta_L^S, \tag{5.14}$$

and

$$(\beta_G)^2 = \left(\beta_G^I\right)^2 + \left(\beta_G^S\right)^2, \tag{5.15}$$

using the well known relation for addition of peak integral breadths for Lorentz- and Gauss functions respectively. By the assumption that the instrument part changes while the sample part stays constant, we can now try to fit some power functions with the TEM beam diameter D as the variable, to the instrument parts of both these equations. In figure 5.6 the fitted curve and its deconvolutions into Gauss and Lorentz is shown.

As an example, in figure 5.7, the calibration series is shown again along with measured series of a CVD grown CNT and one grown by arc-discharge. In figure (b) the sample Lorentz part is shown for each series, showing that this remaining part is indeed constant, after removing instrument contributions. The mean value of such a set of deconvoluted sample Lorentz breadths β_L^S can then be used in equation (5.13) to estimate crystallite size.
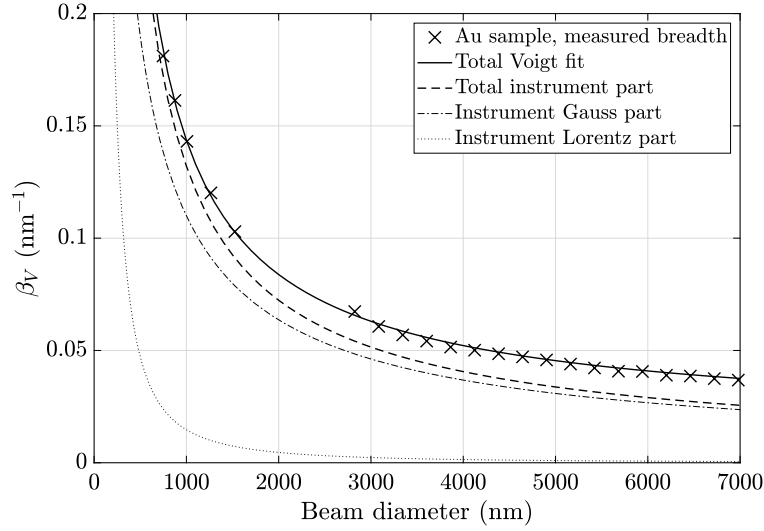
Figure 5.6: A measurement of integral breadth on an Au sample plotted versus TEM beam diameter. The data was fitted with a Voigt function. The constant contribution to the breadth was taken out to reveal the instrument part, consisting of the convolution of a Gauss- and a Lorentz function, which are also shown.

5.1.4   Error estimation

A quantitative analysis of the measuring error for each peak measurement or the derived standard error for composite value calculated from a series of measurements was not done in this dissertation. However, a qualitative discussion on the bounds of measurements and sources for error is possible.

It is clear that taking a series of peak integral breadths for different TEM beam diameters lowers the standard error of the final result. For the calibration sample seen in figure 5.6 we can see points measured in the span of about 700–7000 nm which gives a high degree of accuracy for the underlying sample contributions to the peak breadth. For the series measured on CNTs seen in figure 5.7 however, there are less points of measurement (5 for the arc-discharge and 4 for the CVD) with smaller spans (1000–3500 nm for arc-discharge and 1500–3200 nm for CVD), and the points also deviate from the fitted lines more. This stems from the fact that the CNTs are narrow compared to the flat and wide calibration sample, which inherently will lower the intensity of diffraction, thus rendering a low signal-to-noise ratio. Furthermore, as can also be seen in figure 5.7, the tubes are of lower crystallinity (the value for β_L^S is higher)
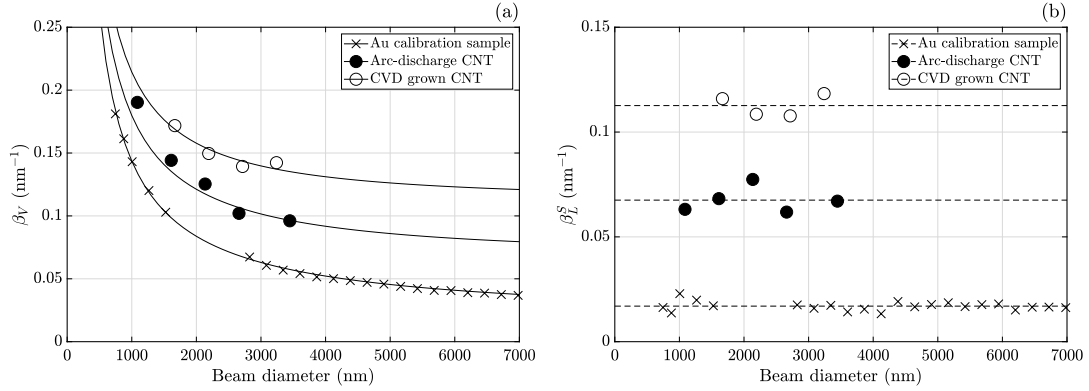
47

Figure 5.7: (a) Integral breadths of the Au calibration sample, a MWCNT grown by arc-discharge and a CVD-grown MWCNT. (b) The Lorentz part of the integral breaths for all three samples. The dashed lines indicate the mean value of each set.

which also means a weaker signal. For wide TEM beams, the signal becomes too weak to measure, as it is obfuscated by noise. The pixel resolution on the camera is also a limitation here, if peaks become so narrow that they are only a few pixels wide. It is also not possible to increase exposure time too much in order to compensate for this, since there is thermal drift making the sample move slightly, blurring the image.

On the other hand, contracting the beam diameter too much the instrument contributions become very large compared to the sample signal, which also makes results less accurate. The uncertainty for individual points of measurement is thus highly dependent on the TEM beam diameter, and for the more narrow and/or low crystallinity tubes the window of beam diameters that is usable for measurement is quite small.

For the particular combination of TEM, camera and the specific samples used in this dissertation, the optimal span of the TEM beam diameter for accurate measurement was found to be around 1500–4000 nm. Keeping within this span, increasing the number of points-of-measurement will increase the accuracy of the final result.

5.2 Electrical resistance

5.2.1 Model for electrical conduction

Electrical conduction was modeled by assuming electron transport in only the outermost CNT layer. For conduction in a two-dimensional medium, such as a single layer of a CNT, it does not make sense to talk about resistivity as one would for a macroscopic conductor. In this case the relevant quantity is instead the total sheet resistance R_s^{tot} of a square sheet in the tube layer. One side of such a sheet is the tube's circumference, so we focus on the resistance of a section of the tube layer with a length equal to πd_o, where d_o is the tube diameter, which turns the "unfolded" sheet of graphene that makes up the cylinder of the tube section into a square. This results in the expression

$$R_s^{\text{tot}} = R_l \cdot \pi d_o, \tag{5.16}$$

where R_l is the linear resistance of the outermost tube layer as measured along the tube.

The linear resistance R_l of a quasi-one-dimensional conductor is defined as its electrical resistance per unit length. To calculate R_l the measured point resistance R_p at each point of contact was plotted versus the length l_p between the main sample and the contact point and a linear fit was made, assuming

$$R_p = R_l \cdot l_p + R_c, \tag{5.17}$$

where in this case the fitting parameters R_l represents the linear resistance of the outermost tube layer and R_c is the total sum of contact resistances between the main sample, the specific tube and the probe electrodes. A typical example of this is shown in figure 5.8.

To connect linear resistance and total sheet resistance with crystallinity, the conducting outer tube layer was modeled[1] to consist of a number of parallel

---

[1] It should be noted that each grain boundary chain is connected with its two neighboring chains at every grain, which impacts the overall resistance. However, for sufficiently long distances between electrodes the voltage difference between parallel conduction chains tends to zero, meaning there is no current between grains across the tube, only along it.
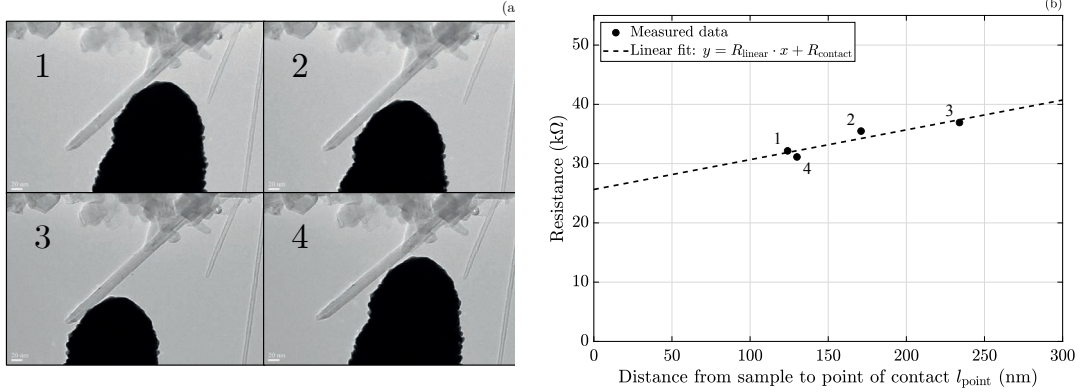
Figure 5.8: (a) Example of measurements along a CNT. Each point of contact is numbered chronologically. (b) The corresponding linear fit of the numbered measured points. The slope of the line corresponds to the linear resistance R_l of the tube outermost layer and the intersection with the y-axis to the total contact resistance R_c of the measurement setup.

connected channels N_p, and each such channel consists of a serial connection of graphene-like grains interconnected by resistive boundaries, as shown in figure 5.9. The number of grains and boundaries in a section of the tube which is l_{tot} long was denoted N_s.

The grains were assumed to have a constant sheet resistance R_s and the boundaries between grains a constant resistance ρ_b divided by the length of the boundary l_b. The resulting expression for the linear resistance of a section of tube was

$$\frac{1}{R_l \cdot l_{tot}} = \frac{N_p}{N_s} \cdot \frac{1}{R_s + \frac{\rho_b}{l_b}}. \tag{5.18}$$

The number of parallel chains N_p in a tube can be approximated[2] by the tube circumference divided by the effective grain size given by $N_p = \pi d_o / L_a$, and the number of grains and boundaries in each chain by the tube section length divided by grain size $N_s = l_{tot} / L_a$.

The length of the boundary between each individual grain of course varies with

---

[2]Note that the number N_p can not physically be smaller than 1, which is the case when the crystallite size spans the entire tube circumference, and there is only one serial chain of crystallite grains. For the specific batch of CNTs used in this work a sufficiently large effective grain size L_a was never found for this to occur, but for larger crystallite size compared to tube diameter this problem should be corrected for.
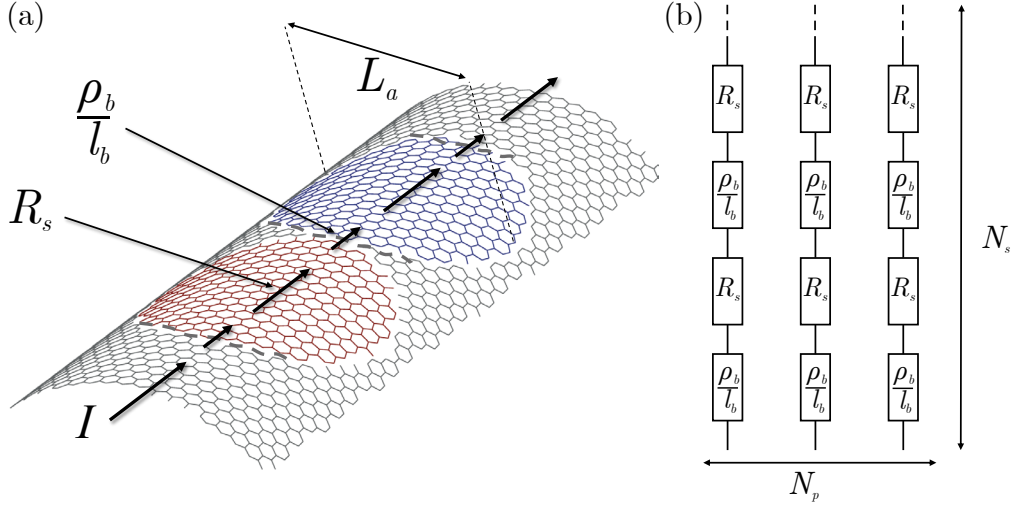
Figure 5.9: (a) Schematic figure of the conduction model where R_s is the within-grain sheet resistance, ρ_b is the boundary resistivity, l_b is the boundary length and L_a is the grain size. Two differently oriented crystallite grains are highlighted within the tube wall. (b) Schematic in terms of resistors where N_s is the number of resistor couples R_s and ρ_b/l_b in the tube section, and N_p is the number of such resistor chains around the circumference of the tube.

the size and shape of the grains. However, we may assume that the average boundary length between grains is directly proportional to the average grain size, that is $l_b = c \cdot L_a$, where c is a dimensionless constant close to 1 depending on grain shape geometry. Assuming we can approximate the grain shapes by squares, we can take this constant to be exactly 1, resulting in $l_b = L_a$. The length of the tube section cancels out, and we obtain an expression for the linear resistance

$$R_l = \frac{1}{\pi \cdot d_o} \cdot \left(\frac{\rho_b}{L_a} + R_s \right). \tag{5.19}$$

Finally, by moving the factor πd_o to the left hand side, and combining it with equation (5.16), we get an equation for the outermost layer total sheet resistance R_s^{tot}, given by

$$R_s^{\text{tot}} = \frac{\rho_b}{L_a} + R_s, \tag{5.20}$$

which is valid for a specific CNT given its material parameters.

Equation (5.20) shows the dependence between the sheet resistance of an individual MWCNT wall and its diameter and crystallite size, given the two

material specific parameters sheet resistivity R_s and boundary resistivity ρ_b, and can be thought of as a "scaling law" for MWCNT outer wall conduction analogous to the scaling law derived for polycrystalline graphene in [106] and further explored in [107]. The problem now becomes to identify the material parameters sheet resistivity R_s and boundary resistivity ρ_b. It is very important to note that these two parameters are not necessarily identical for all carbon nanotubes, but should instead be used to classify tubes of different levels of quality.

5.2.2 Error estimation

A statistical analysis of the variation in resistance during the hold phase of the anneal was made, along with analysis of the quadratic errors in the fitted lines for the linear resistances, in order to derive an estimation of the standard error of these approximations.

Standard deviation of point resistance measurements

A statistical analysis including 90 different annealing instances was done in order to analyze the behavior of the point resistance during the three anneal phases. 81% of anneals had a lower resistance in the last two seconds of the annealing hold phase compared to the first two, with a mean drop of 3.3%. After the big initial drop, the drop in resistance decreased for each two second interval to the next in the 10 second hold, and was on average 0.1% going from time span 6–8 s. to 8–10 s.

The variance in resistance of the hold phase was also analyzed. Initially, the variance is high, and some amount of variance in resistance remains throughout the hold phase, but drops drastically after the first few seconds. In the first two second interval the standard deviation from the mean was found to be over 3 kΩ, while for all subsequent two second intervals of the hold phase, the standard deviation was below 1 kΩ, as shown in 5.10. Since the resistance seems to reach a steady state after the initial high variance, the first two seconds of the hold phase were excluded, and the standard deviation of the re-

maining 8 seconds was 1.3 kΩ. The analysis shows that the contact resistance is initially high and unstable, as seen in figure 4.5 (a), significantly lowered and stabilized by the end of the increasing phase of the anneal, and remains very stable after the first two seconds of the hold phase. These uncertainties can be interpreted as an instability in contact resistance induced by Joule heating. For low bias, the contact resistance is completely stable, and the uncertainty in contact resistance is carried over from the preceding anneal.
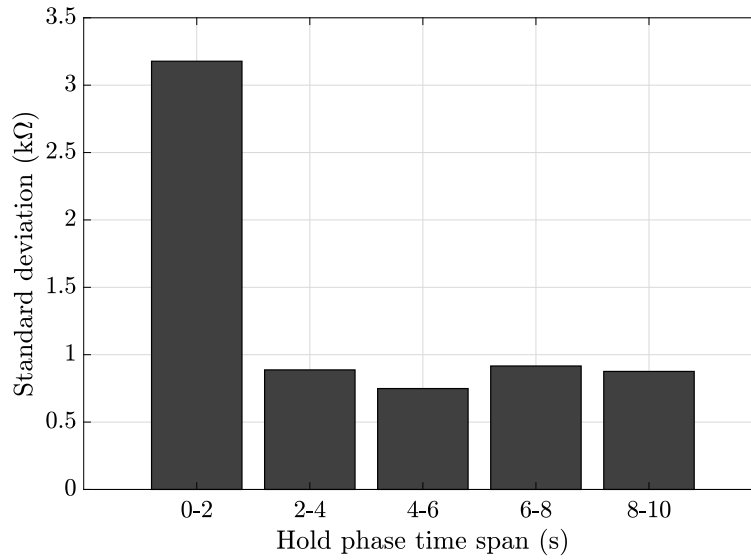

Figure 5.10: A statistical analysis, including 90 annealing instances, of the standard deviation from the mean resistance value during the hold phase of an anneal. The standard deviation is taken in two second intervals, for all 10 seconds of the hold phase.

Apart from the analysis of the anneal phases, the deviation from linearity when using equation (5.17) to calculate linear resistance was looked at. In a statistical analysis including 82 points of resistance measurement it was found that 51% of values for R_p deviated less than 2 kΩ from the value predicted by R_l, 63% deviated less than 3 kΩ and 70% deviated less than 5 kΩ.

The two methods of analysis display a similar standard deviation, however with slightly more variance in the linear resistance analysis. This added variance may have more than one cause. One explanation is that inhomogeneity in the tubes make the assumption of a linear resistance in the tube section less accurate, adding to the errors there. Another explanation is that contact resistance may scale with the total measured resistance of R_p, making it larger

for low bias measurements, and thus scaling the standard deviation up along with it. The median of the ratio between low bias measured resistance and the preceding high bias resistance measured while annealing was found to be about 2, which would scale standard deviation for low bias up to 2.6 kΩ. The idea of a contact resistance which is relative to the total resistance was contradicted however, as another statistical analysis showed there was no significant dependence between standard deviation and resistance magnitude during annealing hold phases, even though the span of annealing hold phase resistance was 20–120 kΩ, clearly overlapping the span of low bias measured resistance. Furthermore, no significant dependence between low bias resistance and deviation from R_l prediction was found. Thus, both methods of analysis indicate that measurements have an absolute variance, rather than relative. For the measurements of R_p in this dissertation, an estimated constant standard deviation of 3 kΩ was used.

Measuring error of linear resistance calculations

For a given standard deviation of R_p we can calculate the measuring error for linear resistance R_l, here denoted $\text{SE}(R_l)$. The parameters that influence the accuracy are the standard deviation of a single point measurement denoted $\text{SD}(R_p)$, the number of points measured n and the total length of the CNT section being measured, denoted l_{tot}, which equates to the range of l_p. There may also be some influence from how the contact points are distributed, however we assume the points are distributed homogeneously over the distance l_{tot}.

To find the dependencies, simulations of measured points with a normally distributed fixed standard deviation was made, and calculating the resulting measuring error in the linear fits while varying the three variables. It was clear that $\text{SE}(R_l)$ is directly proportional to $\text{SD}(R_p)$, and inversely proportional to l_{tot}. For large number of measurements n we could also see that $\text{SE}(R_l)$ was approximately proportional to $1/\sqrt{n}$, which was more accurately determined as $1/\sqrt{n+4}$, fitting better for small values of n, which was the case here. This

lead to a final expression given by

$$\mathrm{SE}\left(R_l\right) = 3.5 \cdot \frac{\mathrm{SD}\left(R_p\right)}{l_{\mathrm{tot}} * \sqrt{n+4}},$$ (5.21)

where $\mathrm{SD}\left(R_p\right)$ is in kΩ, l_{tot} is in μm and $n \geq 2$. The simulations and fitted curves for n and l_{tot} are shown in figure 5.11.
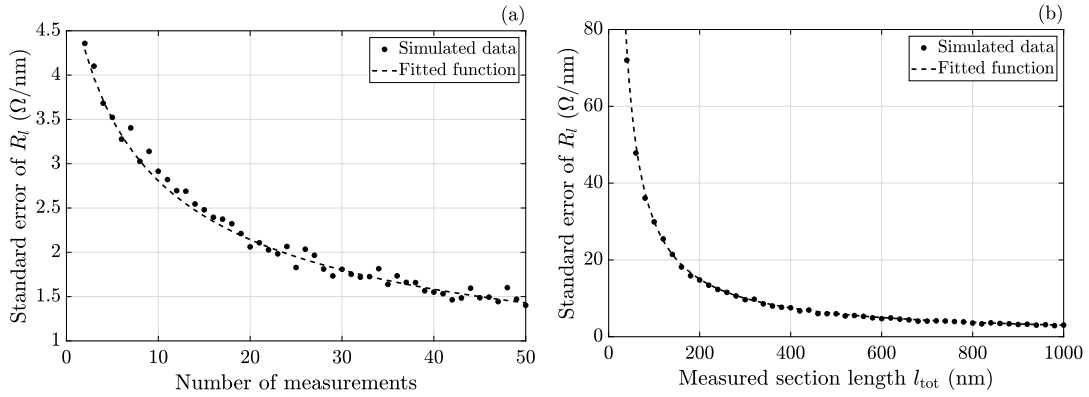

Figure 5.11: Each point is a simulated value, over 500 iterations, of the standard error of R_l given a constant standard deviation $\mathrm{SD}\left(R_p\right) = 3$ kΩ. In (a) each point of measurement was distributed randomly over a length of $l_{\mathrm{tot}} = 1000$ nm and the number of measurements was varied. The dashed line in (a) corresponds to the fitted function in (5.21). In (b) the number of measurements was 10 and the length of measurement l_{tot} was varied. (b) is plotted with logarithmic axes. The dashed line in (b) corresponds to a fit of $1/l_{\mathrm{tot}}$

5.2.3 Influence of tube chirality

For carbon nanotubes with and ideal atomic structure, i.e. perfect crystallinity, the electrical conductivity is predicted to depend on tube chirality. Depending on the way the tube is "rolled up" it obtains different conductive properties, where some tubes are metallic conductors which in essence have a zero linear resistance, while some tubes are semi-conductors. The number of conducting channels for multi-walled tubes also depend on tube diameter and the bias voltage applied. Since tube chirality was not determined in this study, its possible influence had to be estimated.

By using the equations given by Kashcheyevs et. al in [108], which were based on the Dirac cone approximation of the conducting band energy of graphene

nearby the Fermi points, combined with the Landauer–Buttiker formalism, the number of conducting channels of metallic- and semi-conducting CNTs was calculated and compared at the maximum bias voltage used in this study of 5 mV, shown in figure 5.12. The results show that for MWCNTs with a diameter larger than about 10 nm the number of conducting channels differ by less than a factor of two between metallic and semi-conducting tubes, meaning that the problem is relatively small (much smaller than the two orders of magnitude we see in our results on conductivity, shown in chapter 6) when dealing with MWCNTs or large diameter SWCNTs, but may come into play for more narrow tubes.
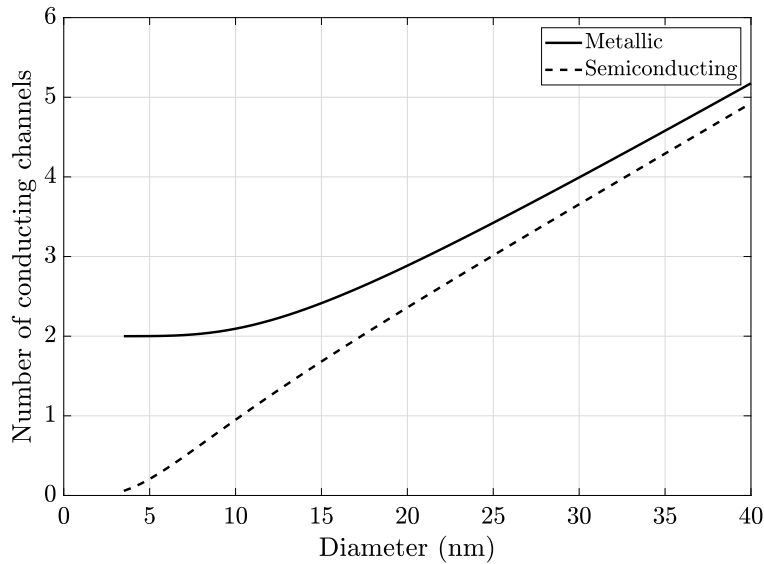
Figure 5.12: Number of conducting channels for undoped metallic and semiconducting tubes calculated at room temperature for 5 mV bias voltage.

5.3 Mechanical stiffness

Previous research on the mechanical stiffness of CNTs has shown large differences depending on the quality and production method of the samples [9, 25]. As a continuation of the work done by Henrik Jackman and Krister Svensson, described and summarized in Jackman's doctoral thesis from 2014 [8], measurements of crystallinity were done on the same very sample batches of CNTs that the original research was made on. In the original studies, one of the

properties measured was the Young's modulus E, which corresponds to the bending stiffness of the tubes when force is applied lengthwise. By using the method for determination of crystallinity described in sections 4.2 and 5.1, the mean values of crystallite size for the sets of differently produced CNTs were obtained. A dependency of Young's modulus E on crystallite size L_a was established, and the results are presented in chapter 6.

Chapter 6

Results and discussion

The development of the methods for measurement and analysis described in chapters 4 and 5 is one of the main results of this dissertation, but it is not the only one. Measurements of crystallinity and linear resistance of CNTs both revealed some new and interesting facts, which are described here, and in more detail in the articles included in the dissertation.

6.1   Young's modulus and CNT production method

The measured integral breadths β_L^S of CNTs from an arc-discharge sample batch and a CVD sample batch were plotted against tube diameter, in order to show there was no discernible diameter dependence of the peak breadth, as is shown in figure 6.1 (a). The data points were grouped by production method, showing a clear difference in the mean value of each set. In figure 6.1 (b) the integral breadths have been put into equation (5.13) and the corresponding values of L_a are plotted, which shows the mean crystallite size for the arc-discharge batch to be 18.6 ± 3.3 nm and the mean value for CVD to be 5.6 ± 1.6 nm, at a 95% confidence level, indicating a clear difference in crystallinity.

The mean values for each group were plotted versus the two previously measured mechanical properties Young's modulus E and the critical strain denoted l_{cr}, as is shown in figure 6.2, together with a visual guide of a plausible variable dependence, shown as a dashed line.

The results show a clear difference in the average crystallite sizes of the two materials. For a tube grown by arc-discharge, with the found average crystallinity of this set, and with a typical outer diameter of about 10 nm, the crystallite size would be enough to encompass more than half the circumference
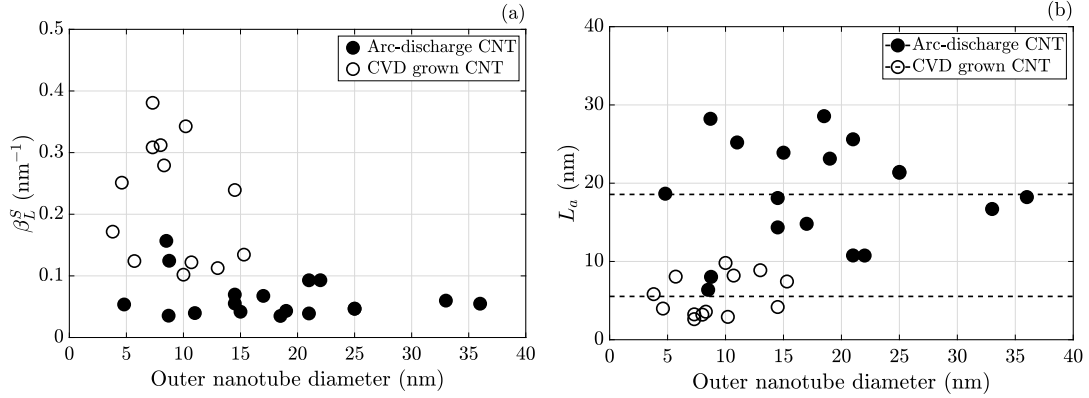
Figure 6.1: (a) Deconvoluted integral peak widths and (b) calculated crystallite sizes, plotted versus outer nanotube diameters. Values for arc-discharge growth are shown as filled circles and values for CVD growth as empty circles. The mean values of each grouped material type is indicated by a dashed line in (b).
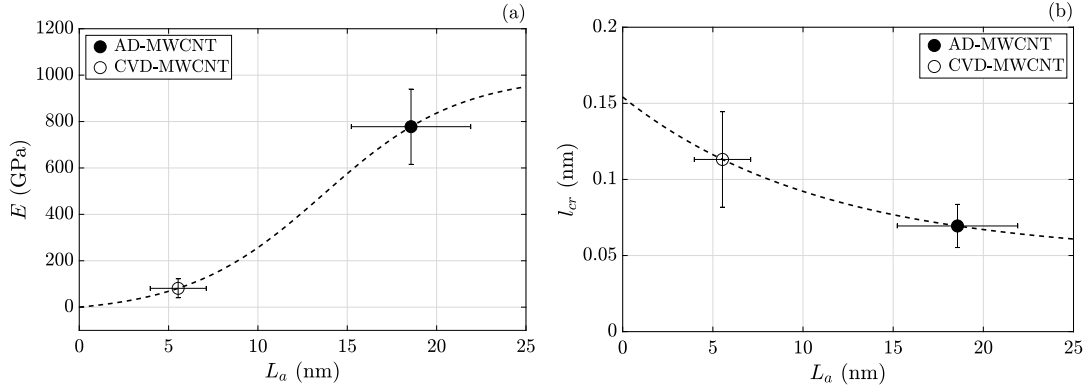

Figure 6.2: (a) Mean values of axial Young's modulus E vs crystallite size L_a, grouped by material. (b) Mean values of the critical length l_{cr} vs crystallite size L_a, grouped by material. A visual guide of a plausible variable dependence is shown as a dashed line and error bars indicate the 95% confidence interval assuming a t-distribution.

of the outermost tubes. This enables the formation of continuous graphene-like cylinders, or cylinder segments, which constitute the walls of the tubes. In contrast, the very small crystallite sizes for CVD grown materials would be much smaller than the tube circumference, implying that here the walls are made from a patchwork of small graphene-like grains with different orientations. The effect these differences have on mechanical behavior is clearly shown in the study, and tubes created with these two production methods should be treated as two distinctly different materials. A more in depth analysis of this can be found in publication I: "Quantifying crystallinity in carbon

nanotubes and its influence on mechanical behaviour" [109] and more information about the studies of the mechanical properties E and l_{cr} can be found in [25] and [9].

6.2   Linear resistance and its dependence on crystallinity

Initially the study on the influence of crystallinity on the electrical properties of CNTs was going to compare production methods, similar to what was done for mechanical properties. However, during the first phase of the study on arc-discharge MWCNTs there was an unexpected and interesting result; within the same batch of CNTs, produced by the same method, a sharp threshold and a drastic shift in linear resistance at a critical value for the mean crystallite size L_a was found, shown in figure 6.3 (a), and for this reason the study was refocused to only include the tubes grown by arc-discharge. Conversely, there was no significant dependence found between linear resistance and outer tube diameter, as shown in figure 6.3 (b), which is in line with the discussion on tube chirality from section 5.2.3.
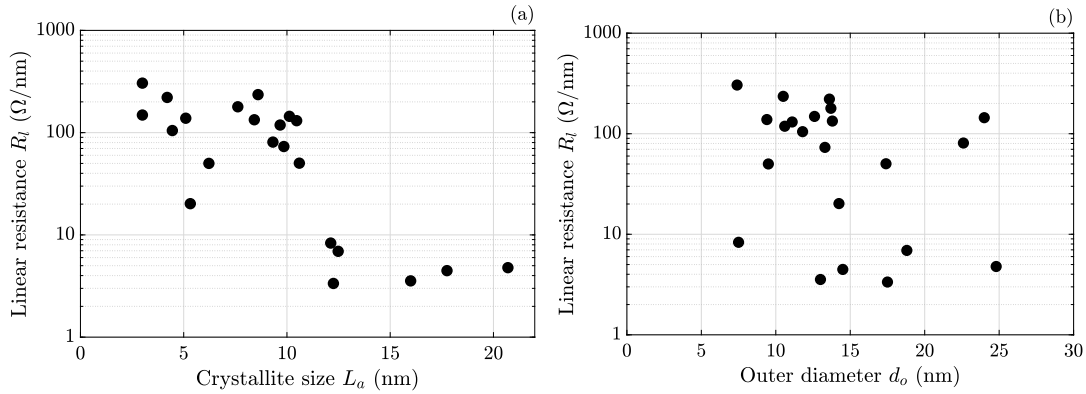
Figure 6.3: Linear resistance R_l plotted versus (a) the mean crystallite size L_a, and (b) the outer tube diameter d_o, with a logarithmic y-scale.

At room temperature this critical threshold point was found to be at a crystallite size of around 11 nm and the measurements were split into two regions, $L_a < 10$ nm and $L_a > 12$ nm. For each group, the within-grain sheet resistance R_s and between-grain border resistivity ρ_b was extracted by calculating the total sheet resistance R_s^{tot} for each CNT within each region and fitting it

linearly against $1/L_a$ in accordance with equation (5.20). The linear fits for both regions is shown in figure 6.4, and the fitted parameters are shown in in table 6.1.

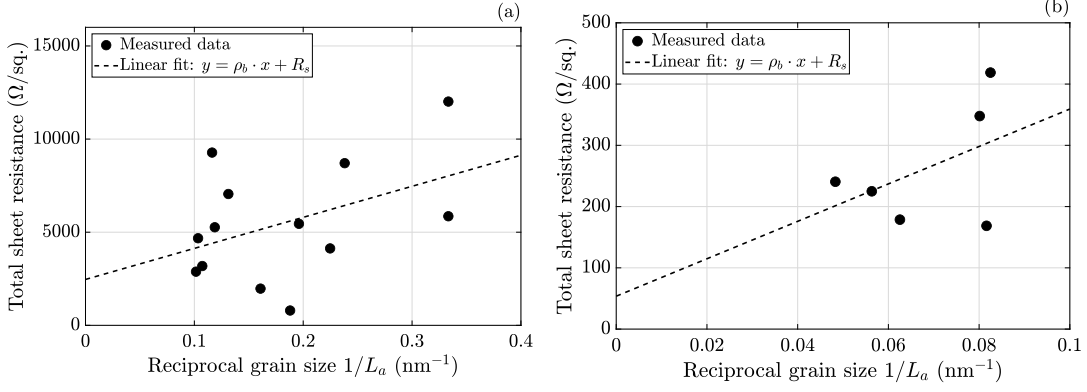*Figure 6.4: Linear fit of the total sheet resistance against $1/L_a$ for (a) the region $L_a < 10$ nm, and (b) the region $L_a > 12$ nm, according to equation (5.20). The slope of the lines correspond to the boundary resistivity ρ_b and the intersection with the y-axis corresponds to the within-grain sheet resistance R_s for each region respectively.*

Table 6.1: The fitted parameters for both regions of grain size.

CNT grain size	R_s	ρ_b
$L_a < 10$ nm	2.5 kΩ/□	17 Ω·µm
$L_a > 12$ nm	54 Ω/□	3 Ω·µm

The large change in conductivity at the critical crystallite size is thus explained by a significant increase in both grain sheet resistance and boundary resistivity. Comparing the two regions we see that within-grain sheet resistance is almost 50 times smaller in the high crystallinity region compared to the tubes with lower crystallinity. The boundary resistivity in the high crystallinity region is also about 5 times smaller, indicating that the boundaries themselves also deteriorate in electrical conductivity together with the lower crystallinity within the grains.

By taking the reciprocal of equation (5.19) the linear conductance G_l was calculated, given by

$$G_l = \frac{\pi d_o L_a}{\rho_b + L_a R_s}. \tag{6.1}$$

The two regions of crystallinity was now tied together by creating a "universal curve fit", using the parameters from table 6.1 for the two regions separately, with a smooth curve-transition using and S-shaped function, given by

$$G_{\text{universal}}(x) = G_1(x) + S(x) \cdot (G_2(x) - G_1(x)), \qquad (6.2)$$

where G_1 and G_2 denote the conductance for the two regions, and S is given by

$$S(x) = \frac{1}{2}\left[1 + \tanh\left(\frac{x - x_0}{w}\right)\right], \qquad (6.3)$$

with the parameters $w = 0.55$ nm and $x_0 = 11$ nm. Since G_l also requires a value for d_o we have used the mean diameter 14 nm to create the universal curve, shown in figure 6.5. To illustrate the influence of the tube's outer diameter, the curve was also plotted using the extreme values found in the study, $d_o = 7$ nm and $d_o = 25$ nm, displayed with dash-dotted lines.
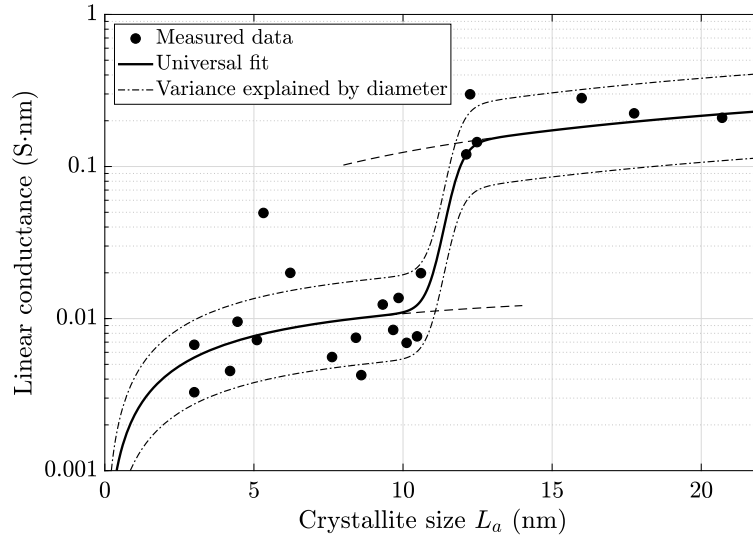
Figure 6.5: Linear conductance of CNTs vs grain size measured at room temperature and fitted with a "universal curve". Each region was plotted according to equation (6.1) with parameters taken from table 6.1, and the transition from one curve to the other was done by using equation (6.2) and (6.3). Since equation (6.1) also depends on the tube outer diameter d_o, the curve was plotted with the mean, minimum and maximum values found in the study, which was 14 nm (solid line), 7 nm and 25 nm (dash-dotted lines) respectively. For each region the curve is slightly extended beyond its valid interval (dashed line) to indicate the continued shape.

We find that the influence of crystallinity is even greater on electrical con-

duction than on mechanical stiffness and critical length, found in the former study. The effect is interpreted as a result of quantum confinement and edge-effects in the individual crystallites, which create band gaps that are large enough in order to greatly reduce the electrical conductance at room temperature. Even within the same batch produced by the higher crystallinity method of arc-discharge we find large differences in conductivity, connected to differences in crystallinity, which may be part of the explanation for the wide variety of results in linear resistivity observed for MWCNTs previously in the literature [14, 16, 17]. More detail this can be found in publication III: "Influence of crystallinity on the electrical conductivity of individual carbon nanotubes" [110].

6.3 Crystallinity method

A method was developed that provides quantitative information about the crystallinity of MWCNTs. The method relies on analyzing straight sections of individual tubes with detailed analysis of diffraction spots in positions and directions that are not influenced by the curvature of the tubes. By carefully mapping the optimal diffraction focus for different TEM beam diameters, and by fitting the broadening stemming from the TEM-beam to a power function, the instrument contribution can be separated from the total contribution using a series of measurements at different beam diameters. This will then provide a reliable measure of the inherent sample broadening effects and the effective crystallite sizes. This method should be applicable also to other, non-carbon, tubular structures. Some of the main advantages compared to other determination methods of crystallinity or defect density are that the analysis can be done on a small segment of an individual nanotube, and that it can also be done in the same session as the measurement of its mechanical or electrical properties.

Another example of how the method can be used to measure the effect of thermal treatment on CNTs, and how the crystallinity may be improved by such methods, is found in publication IV: "Effects of high temperature treatment of carbon nanotube arrays on graphite: increased crystallinity, anchoring and
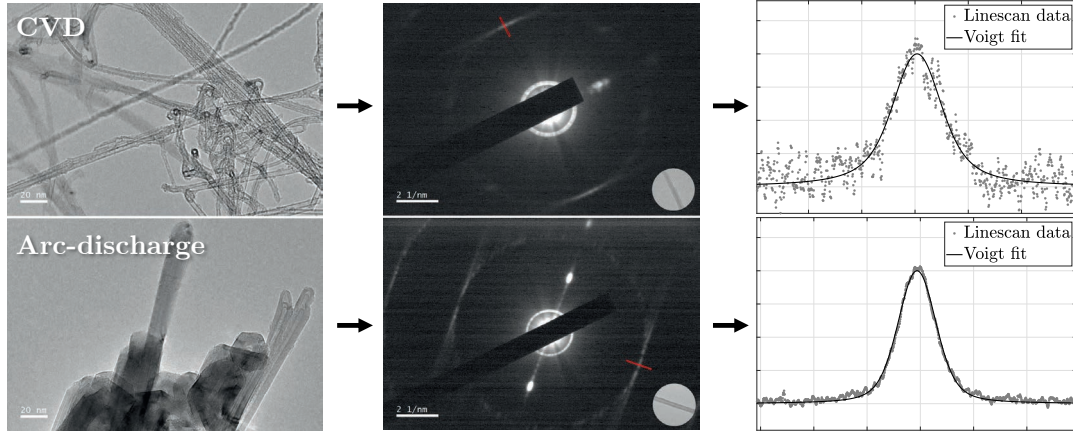
Figure 6.6: With the method that was developed here, the crystallinity of carbon nanotubes produced by different techniques could be determined and compared. In the TEM images to the left, the CVD tubes on the top row can qualitatively be seen to be of lower crystallinity than the bottom row tubes produced by arc-discharge. The diffraction images seen in the center of the figure also show a difference in overall sharpness. The difference is finally quantified in the rightmost images, by measuring the peak integral breadth of the diffraction peaks corresponding to atomic lattice spacing. The linescan data is taken from the two narrow rectangles seen in the diffraction images.

inter-tube bonding" [35]. In this article, the TEM diffraction method is used in tandem with Raman spectroscopy, which is valid for crystal sizes of about 2–10 nm [57]. The method developed here using the Scherrer equation has a theoretical upward limit of about 200 nm [111], limited further in practice for the studies described here to about 100 nm, and a lower limit due to instrumental limitations such as signal-to-noise and resolution of approximately 3 nm. In the overlapping range between the two methods, the results were found to be very similar, which further confirms the accuracy and validity of the Scherrer-based method.

6.4 Linear resistance method

A method for characterization of the electrical resistance of the outermost tube wall of MWCNTs was developed. The analysis showed that two-probe methods can provide a very accurate measure of the linear resistance in carbon nanotubes. By annealing with joule heating the contacts have a low and stable enough contact resistance in order to provide accurate estimations of the

linear resistance. The accuracy and repeatability of the method is very high, and we find a standard deviation of around 3 kΩ for each point of contact. With a suitable number of contact points and a large enough spread in the positions, it is possible to characterize the linear resistance with a high accuracy even down to only a few kΩ/μm. The exact number of contact points and distance to measure over depends on the standard deviation of each point measurement, so a general prescription can not be given, however for similar values of variance as seen here we suggest the use of about 8 or more points, over a distance of 1 μm or longer.

By combining the methods for determination of linear resistance with a characterization of crystallinity, it was found that an apparent spread in the linear resistance values can be explained by differences in the material properties of individual tubes, rather than in the methods themselves. Taking the data shown in figure 6.3, and using equation (5.21) to calculate the standard error of each data point, based on the actual measured section length l_{tot}, the number of measurements n and using an estimated standard deviation of each point measurement $\mathrm{SD}(R_p)$ of 3 kΩ, we can plot the data with error bars, shown in figure 6.7.
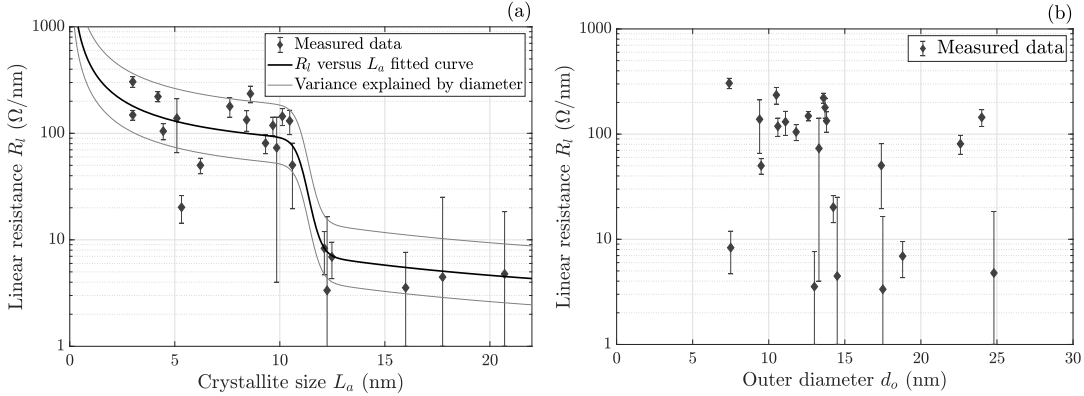
Figure 6.7: (a) Linear resistance R_l plotted versus the crystallite size L_a. The fitted curve was plotted using the mean value of the outer diameter of the dataset, which was 14 nm. The curves shown above and below were plotted using the two extreme values of the outer diameter found, to illustrate the variance explained by tube diameter. (b) Linear resistance plotted versus the outer diameter d_o. The error bars of both figures indicate the estimated standard error of R_l, using equation (5.21).

From inspection of figure 6.7 (a), we find that the correlation described by

equation (5.19) holds, even after taking into account the uncertainty in R_l as calculated before, indicated by the error bars. Instead, looking at figure 6.7 (b), it is clear that tube diameter alone can not account for the spread in linear resistance seen in the data, even when taking into account the measurement error margins as before.

The study also showed that the tube layer can be modeled as a patchwork of crystallite grains connected by boundaries. A scaling model for the electrical conductivity within a single layer of a CNT was suggested, which connects its electrical conductivity with the crystallite size and tube diameter. It also links the overall sheet resistance of the outermost tube wall to its intrinsic material parameters R_s and ρ_b which correspond to the crystallite grain sheet resistance and grain boundary resistivity respectively. The method is described in greater detail in publication II: "Accurate determination of electrical conductance in carbon nanostructures" [112].

The accuracy of the method is thought to be sufficiently high to warrant inclusion in the general toolbox needed for the characterization and classification of carbon nanotube materials, as a first step towards a measurement standard.

Chapter 7
Conclusion and outlook

The work described in this dissertation has led to the development of new methods for characterizing carbon nanotubes. The ability to accurately and quickly quantify the crystallinity of an individual CNT, and even a small section of one, inside a TEM has great possibilities. Combined with the two-point electrical measurement methods and models for analysis to characterize the linear resistance of CNTs presented here, as well as with other TEM characterization such as bending stiffness, the usefulness of the method becomes even clearer. Here, and in the publications from which this dissertation builds, the necessary steps for these methods to be implemented have been presented in detail, including instructions for calibration, methods for electrical annealing, models for analysis as well as error estimates and suggestions for measurement error minimization.

There are no claims that these techniques are the most accurate available in all cases, nor that they should be the first choice in every situation, however the overall ease-of-use, versatility, and their reasonable accuracy make them a powerful new addition to the nanotube experimentalist's toolbox. The proposed method is believed to be accurate enough in order to serve as a first step towards a measurement standard, and hence as one of several tools needed for the characterization and classification of carbon nanotube materials.

Apart from the methods for measuring and models for analysis, there were also some new and unique results and conclusions from the data. It is clear that "carbon nanotubes" is not a single material, but rather an assortment of materials. Different production methods result in vastly different levels of crystallinity, and the electrical and mechanical properties are greatly affected by these differences. Even within the same batch made with the same techniques there are differences in crystallinity that can result in electrical resistance vari-

ations of two orders of magnitude, or more. Single-walled CNTs are likely very different from multi-walled, especially those with high crystallinity where the small tube diameter and chirality differences will have a large effect on linear resistance, while the lower crystallinity tubes will likely not be affected very much by differences in chirality and diameter.

In this work it was shown that outermost wall conduction for MWCNTs at low bias voltage may be modeled as a patchwork of crystallite grains connected by boundaries, and that the overall conductivity of the tube wall is greatly influenced by even small changes in this structure. In future work, the model should be combined with existing models for multi-shell conduction, and its validity should be tested for higher bias voltages as well as for smaller sized, and single-walled tubes.

In publication IV, the method for determination of crystallinity described in this dissertation was used to confirm that it is possible to increase crystallinity in CVD grown tubes by thermal treatment, resulting in piecewise straight sections of high quality separated by structural defects. The effects of treatment on the mechanical and electrical properties of the tubes can be inferred by the suggested dependencies on crystallinity presented in this work, but should in the future be confirmed by direct measurement, coupled with crystallinity data from the very same tubes. Furthermore, it would be very interesting to investigate whether post-treated CVD tubes can achieve properties similar to the higher crystallinity tubes made by arc-discharge, or if there is a cap on how far the crystallinity can be improved for tubes that initially have very small crystallite sizes. This type of quantitative data can be used in order to classify carbon nanotube materials in terms of their crystallinity and physical properties, and thereby provide reliable source materials for industrial applications.

References

[1] Treacy, M.M.J., Ebbesen, T.W., and Gibson, J.M. Exceptionally high Young's modulus observed for individual carbon nanotubes. *Nature*, 381(6584):678–680, 1996.

[2] Dresselhaus, M.S., Dresselhaus, G., Charlier, J.C., and Hernández, E. Electronic, thermal and mechanical properties of carbon nanotubes. *Philosophical transactions. Series A, Mathematical, physical, and engineering sciences*, 362(1823):2065–98, 2004.

[3] Salvetat, J.P., Kulik, A.J., Bonard, J.M., Briggs, G.A.D., Stöckli, T., Méténier, K., Bonnamy, S., Béguin, F., Burnham, N.a., and Forró, L. Elastic Modulus of Ordered and Disordered Multiwalled Carbon Nanotubes. *Advanced Materials*, 11(2):161–165, 1999.

[4] Lukić, B., Seo, J., Couteau, E., Lee, K., Gradečak, S., Berkecz, R., Hernadi, K., Delpeux, S., Cacciaguerra, T., Béguin, F., Fonseca, A., Nagy, J., Csányi, G., Kis, A., Kulik, A., and Forró, L. Elastic modulus of multiwalled carbon nanotubes produced by catalytic chemical vapour deposition. *Applied Physics A*, 80(4):695–700, 2005.

[5] Jackman, H., Krakhmalev, P., and Svensson, K. Measurements of the critical strain for rippling in carbon nanotubes. *Applied Physics Letters*, 98(18):183104, 2011.

[6] Zhang, S., Mielke, S.L., Khare, R., Troya, D., Ruoff, R.S., Schatz, G.C., and Belytschko, T. Mechanics of defects in carbon nanotubes: Atomistic and multiscale simulations. *Physical Review B*, 71(11):115403, 2005.

[7] Zhu, L., Wang, J., and Ding, F. The Great Reduction of a Carbon Nanotube's Mechanical Performance by a Few Topological Defects. *ACS Nano*, 10(6):6410–6415, 2016.

[8] Jackman, H. *Mechanical properties of carbon nanotubes and nanofibres*. PhD thesis, Karlstad University, 2014.

[9] Jackman, H., Krakhmalev, P., and Svensson, K. Mechanical behavior of carbon nanotubes in the rippled and buckled phase. *Journal of Applied Physics*, 117(8):084318, 2015.

[10] Che, J., Çagin, T., and Goddard, W.A. Thermal conductivity of carbon nanotubes. *Nanotechnology*, 11(2):65–69, 2000.

[11] Cui, L., Feng, Y., Tan, P., and Zhang, X. Heat conduction in double-walled carbon nanotubes with intertube additional carbon atoms. *Physical Chemistry Chemical Physics*, 17(25):16476–16482, 2015.

[12] Chico, L., Benedict, L.X., Louie, S.G., and Cohen, M.L. Quantum conductance of carbon nanotubes with defects. *Physical Review B*, 54(4):2600–2606, 1996.

[13] Gómez-Navarro, C., Pablo, P.J.D., Gómez-Herrero, J., Biel, B., Garcia-Vidal, F.J., Rubio, A., and Flores, F. Tuning the conductance of single-walled carbon nanotubes by ion irradiation in the Anderson localization regime. *Nature Materials*, 4(7):534–539, 2005.

[14] Bourlon, B., Miko, C., Forró, L., Glattli, D.C., and Bachtold, A. Determination of the Intershell Conductance in Multiwalled Carbon Nanotubes. *Physical Review Letters*, 93(17):176806, 2004.

[15] Tarkiainen, R., Ahlskog, M., Zyuzin, A., Hakonen, P., and Paalanen, M. Transport in strongly disordered multiwalled carbon nanotubes. *Physical Review B*, 69(3):033402, 2004.

[16] Ebbesen, T.W., Lezec, H.J., Hiura, H., Bennett, J.W., Ghaemi, H.F., and Thio, T. Electrical conductivity of individual carbon nanotubes. *Nature*, 382(6586):54–56, 1996.

[17] Bachtold, A., Henny, M., Terrier, C., Strunk, C., Schönenberger, C., Salvetat, J.P., Bonard, J.M., and Forró, L. Contacting carbon nanotubes selectively with low-ohmic contacts for four-probe electric measurements. *Applied Physics Letters*, 73(2):274–276, 1998.

[18] Mtsuko, D., Koshio, A., Yudasaka, M., Iijima, S., and Ahlskog, M. Measurements of the transport gap in semiconducting multiwalled carbon nanotubes with varying diameter and length. *Phys. Rev. B*, 91:195426, 2015.

[19] Tessonnier, J.P., Rosenthal, D., Hansen, T.W., Hess, C., Schuster, M.E., Blume, R., Girgsdies, F., Pfänder, N., Timpe, O., Su, D.S., and Schlögl, R. Analysis of the structure and chemical properties of some commercial carbon nanostructures. *Carbon*, 47(7):1779–1798, 2009.

[20] Arepalli, S., Nikolaev, P., Gorelik, O., Hadjiev, V.G., Holmes, W., Files, B., and Yowell, L. Protocol for the characterization of single-wall carbon nanotube material quality. *Carbon*, 42(8-9):1783–1791, 2004.

[21] Grobert, N. Nanotubes – grow or go? *Materials Today*, 9(10):64, 2006.

[22] Grobert, N. Carbon nanotubes - becoming clean. *Materials Today*, 10(1-2):28–35, 2007.

[23] Potter, K. *Introduction to Composite Products: Design, development and manufacture*. Chapman & Hall, London, 1996.

[24] de Keijser, T.H., Mittemeijer, E.J., and Rozendaal, H.C.F. The determination of crystallite-size and lattice-strain parameters in conjunction with the profile-refinement method for the determination of crystal structures. *Journal of Applied Crystallography*, 16(3):309–316, 1983.

[25] Jackman, H., Krakhmalev, P., and Svensson, K. Large variations in the onset of rippling in concentric nanotubes. *Applied Physics Letters*, 104(2):021910, 2014.

[26] Monthioux, M. and Kuznetsov, V. Who should be given the credit for the discovery of carbon nanotubes? *Carbon*, 44(9):1621–1623, 2006.

[27] Iijima, S. Helical microtubules of graphitic carbon. *Nature*, 354(6348):56–58, 1991.

[28] Loiseau, A., Launois-Bernede, P., Petit, P., Roche, S., and Salvetat, J. *Understanding Carbon Nanotubes: From Basics to Applications*. Lecture Notes in Physics. Springer Berlin Heidelberg, 2006.

[29] Owens, F. and Poole, C. *The Physics and Chemistry of Nanosolids*. Wiley, 2008.

[30] Kiang, C.H., Endo, M., Ajayan, P.M., Dresselhaus, G., and Dresselhaus, M.S. Size effects in carbon nanotubes. *Phys. Rev. Lett.*, 81:1869–1872, 1998.

[31] Loos, M. Chapter 4 - Production of CNTs and Risks to Health. In Loos, M., editor, *Carbon Nanotube Reinforced Composites*, pages 103–123. William Andrew Publishing, Oxford, 2015.

[32] Sharma, R., Sharma, A.K., and Sharma, V. Synthesis of carbon nanotubes by arc-discharge and chemical vapor deposition method with analysis of its morphology, dispersion and functionalization characteristics. *Cogent Engineering*, 2(1):1094017, 2015.

[33] Arepalli, S. Laser ablation process for single-walled carbon nanotube production. *Journal of nanoscience and nanotechnology*, 4:317–25, 05 2004.

[34] Aravind Kumar Jagadeesan, K.T. and Dhananjeyan, V. *Carbon Nanotubes: Synthesis, Properties and Applications, 21st Century Surface Science - a Handbook*. IntechOpen, 2020.

[35] Hansson, J., Nylander, A., Flygare, M., Svensson, K., Ye, L., Nilsson, T., Fu, Y., and Liu, J. Effects of high temperature treatment of carbon nanotube arrays on graphite: increased crystallinity, anchoring and intertube bonding. *Nanotechnology*, 31(45):455708, 2020.

[36] Chen, Q., Wang, S., and Peng, L.M. Establishing Ohmic contacts for in situ current-voltage characteristic measurements on a carbon nanotube inside the scanning electron microscope. *Nanotechnology*, 17(4):1087–1098, 2006.

[37] Hirsch, A. Functionalization of single-walled carbon nanotubes. *Angewandte Chemie International Edition*, 41(11):1853–1859, 2002.

[38] Ajayan, P.M. and Tour, J.M. Nanotube composites. *Nature*, 447:1066–1068, 2007.

[39] De Volder, M.F.L., Tawfick, S.H., Baughman, R.H., and Hart, a.J. Carbon nanotubes: present and future commercial applications. *Science*, 339(6119):535–9, 2013.

[40] Ajayan, P.M. and Zhou, O.Z. *Applications of Carbon Nanotubes*, pages 391–425. Springer Berlin Heidelberg, Berlin, Heidelberg, 2001.

[41] Cha, S., Kim, K., Arshad, S., Mo, C., and Hong, S. Extraordinary strengthening effect of carbon nanotubes in metal-matrix nanocomposites processed by molecular-level mixing. *Advanced Materials*, 17:1377–1381, 2005.

[42] Bandaru, P.R. Electrical properties and applications of carbon nanotube structures. *Journal of Nanoscience and Nanotechnology*, 7(4-5):1239–1267, 2007.

[43] Paradise, M. and Goswami, T. Carbon nanotubes - production and industrial applications. *Materials and Design*, 28(5):1477–1489, 2007.

[44] Kuzmenko, V., Saleem, A., Staaf, H., Haque, M., Bhaskar, A., Flygare, M., Svensson, K., Desmaris, V., and Enoksson, P. Hierarchical cellulose-derived CNF/CNT composites for electrostatic energy storage. *Journal of Micromechanics and Microengineering*, 26(12), 2016.

[45] Kuzmenko, V., Wang, N., Haque, M., Naboka, O., Flygare, M., Svensson, K., Gatenholm, P., Liu, J., and Enoksson, P. Cellulose-derived carbon nanofibers/graphene composite electrodes for powerful compact supercapacitors. *RSC Advances*, 7(73), 2017.

[46] Gong, H., Peng, R., and Liu, Z. Carbon nanotubes for biomedical imaging: The recent advances. *Advanced Drug Delivery Reviews*, 65(15):1951–1963, 2013.

[47] Jain, N. and Jee Kanu, N. The potential application of carbon nanotubes in water treatment: A state-of-the-art-review. *Materials Today: Proceedings*, 43:2998–3005, 2021.

[48] Kreupl, F., Graham, A., Duesberg, G., Steinhögl, W., Liebau, M., Unger,

E., and Hönlein, W. Carbon nanotubes in interconnect applications. *Microelectronic Engineering*, 64(1):399–408, 2002.

[49] Houska, C.R. and Warren, B.E. X-Ray Study of the Graphitization of Carbon Black. *Journal of Applied Physics*, 25(12):1503–1509, 1954.

[50] Tuinstra, F. and Koenig, J.L. Raman Spectrum of Graphite. *The Journal of Chemical Physics*, 53(3):1126–1130, 1970.

[51] Cançado, L.G., Takai, K., Enoki, T., Endo, M., Kim, Y.A., Mizusaki, H., Jorio, A., Coelho, L.N., Magalhães-Paniago, R., and Pimenta, M.A. General equation for the determination of the crystallite size La of nanographite by Raman spectroscopy. *Applied Physics Letters*, 88(16):163106, 2006.

[52] Lucchese, M., Stavale, F., Ferreira, E.M., Vilani, C., Moutinho, M., Capaz, R.B., Achete, C., and Jorio, A. Quantifying ion-induced defects and Raman relaxation length in graphene. *Carbon*, 48(5):1592–1597, 2010.

[53] Behler, K., Osswald, S., Ye, H., Dimovski, S., and Gogotsi, Y. Effect of Thermal Treatment on the Structure of Multi-walled Carbon Nanotubes. *Journal of Nanoparticle Research*, 8(5):615–625, 2006.

[54] Rao, A.M., Jorio, A., Pimenta, M.A., Dantas, M.S.S., Saito, R., Dresselhaus, G., and Dresselhaus, M.S. Polarized Raman Study of Aligned Multiwalled Carbon Nanotubes. *Physical Review Letters*, 84(8):1820–1823, 2000.

[55] Puech, P., Flahaut, E., Bassil, A., Juffmann, T., Beuneu, F., and Bacsa, W.S. Raman bands of double-wall carbon nanotubes: comparison with single- and triple-wall carbon nanotubes, and influence of annealing and electron irradiation. *Journal of Raman Spectroscopy*, 38(6):714–720, 2007.

[56] Osswald, S., Havel, M., and Gogotsi, Y. Monitoring oxidation of multiwalled carbon nanotubes by Raman spectroscopy. *Journal of Raman Spectroscopy*, 38(6):728–736, 2007.

[57] Mallet-Ladeira, P., Puech, P., Toulouse, C., Cazayous, M., Ratel, N., P, W., Vignoles, G., and Monthioux, M. A raman study to obtain crystallite size of carbon materials: A better alternative to the tuinstra–koenig law. *Carbon*, 80:629–639, 2014.

[58] Jorio, A. and Saito, R. Raman spectroscopy for carbon nanotube applications. *Journal of Applied Physics*, 129(2), 2021.

[59] Belin, T. and Epron, F. Characterization methods of carbon nanotubes: a review. *Materials Science and Engineering: B*, 119(2):105–118, 2005.

[60] Lehman, J.H., Terrones, M., Mansfield, E., Hurst, K.E., and Meunier, V. Evaluating the characteristics of multiwall carbon nanotubes. *Carbon*, 49(8):2581–2602, 2011.

[61] Zhou, O., Fleming, R.M., Murphy, D.W., Chen, C.H., Haddon, R.C., Ramirez, A.P., and Glarum, S.H. Defects in Carbon Nanostructures. *Science*, 263:1744–1747, 1994.

[62] Hashimoto, A., Suenaga, K., Gloter, A., Urita, K., and Iijima, S. Direct evidence for atomic defects in graphene layers. *Nature*, 430(7002):870–873, 2004.

[63] Seyring, M., Simon, A., Voigt, I., Ritter, U., and Rettenmayr, M. Quantitative crystallographic analysis of individual carbon nanofibers using high resolution transmission electron microscopy and electron diffraction. *Carbon*, 116:347–355, 2017.

[64] Bachtold, A., Strunk, C., Schönenberger, C., Salvetat, J.P., and Forró, L. Electrical properties of single carbon nanotubes. *AIP Conference Proceedings*, 442(1):65–68, 1998.

[65] Schönenberger, C., Bachtold, A., Strunk, C., Salvetat, J.P., and Forró, L. Interference and Interaction in multi-wall carbon nanotubes. *Applied Physics A: Materials Science & Processing*, 69(3):283–295, 1999.

[66] Bourlon, B., Glattli, D., Plaçais, B., Berroir, J., Miko, C., Forró, L., and Bachtold, A. Geometrical Dependence of High-Bias Current in Multi-walled Carbon Nanotubes. *Physical Review Letters*, 92(2):1–4, 2004.

[67] Ahlskog, M., Hokkanen, M.J., Levshov, D., Svensson, K., Volodin, A., and van Haesendonck, C. Individual arc-discharge synthesized multiwalled carbon nanotubes probed with multiple measurement techniques. *Journal of Vacuum Science & Technology B*, 38(4):042804, 2020.

[68] Wei, X., Chen, Q., Peng, L., Cui, R., and Li, Y. In situ measurements on individual thin carbon nanotubes using nanomanipulators inside a scanning electron microscope. *Ultramicroscopy*, 110(3):182–9, 2010.

[69] Poncharal, P., Berger, C., Yi, Y., Wang, Z.L., and De Heer, W.A. Room temperature ballistic conduction in carbon nanotubes. *Journal of Physical Chemistry B*, 106(47):12104–12118, 2002.

[70] Kajiura, H., Nandyala, A., Coskun, U.C., Bezryadin, A., Shiraishi, M., and Ata, M. Electronic mean free path in as-produced and purified single-wall carbon nanotubes. *Applied Physics Letters*, 86(12):122106, 2005.

[71] Kajiura, H., Huang, H., and Bezryadin, A. Quasi-ballistic electron transport in double-wall carbon nanotubes. *Chemical Physics Letters*, 398(4-6):476–479, 2004.

[72] Kajiura, H., Nandyala, A., and Bezryadin, A. Quasi-ballistic electron transport in as-produced and annealed multiwall carbon nanotubes. *Carbon*, 43(6):1317–1319, 2005.

[73] Strand, H.U. *Electron Transport Characterization of Multiwalled Carbon Nanotubes*. Master of science, Chalmers Univeristy of Technology, 2007.

[74] Strand, H., Svensson, K., and Olsson, E. Measuring electrical properties of carbon nanotubes using liquid metal immersion, an in situ scanning electron microscopy study. In *EMC 2008 14th European Microscopy Congress 1–5 September 2008, Aachen, Germany*, pages 313–314. Springer Berlin Heidelberg, Berlin, Heidelberg, 2008.

[75] Kobylko, M., Kociak, M., Sato, Y., Urita, K., Bonnot, A.M., Kasumov, A., Kasumov, Y., Suenaga, K., and Colliex, C. Ballistic- and quantum-

conductor carbon nanotubes: A reference experiment put to the test. *Physical Review B*, 90(19):195431, 2014.

[76] de Knoop, L. *Investigation of Iron Filled Multiwalled Carbon Nanotubes*. Master thesis, Chalmers University of Technology, 2005.

[77] de Knoop, L., Svensson, K., Pettersson, H., and Olsson, E. Extraction and Local Probing of Individual Carbon Nanotubes. In *AIP Conference Proceedings*, volume 786, pages 118–123. AIP, 2005.

[78] Wang, Y., Wu, J., and Wei, F. A treatment method to give separated multi-walled carbon nanotubes with high purity, high crystallization and a large aspect ratio. *Carbon*, 41(15):2939–2948, 2003.

[79] Lu, K.L., Lago, R.M., Chen, Y.K., Green, M.L., Harris, P.J., and Tsang, S.C. Mechanical damage of carbon nanotubes by ultrasound. *Carbon*, 34(6):814–816, 1996.

[80] Moonoosawmy, K.R. and Kruse, P. To dope or not to dope: the effect of sonicating single-wall carbon nanotubes in common laboratory solvents on their electronic structure. *Journal of the American Chemical Society*, 130(40):13417–24, 2008.

[81] Williams, D.B. and Carter, C.B. *Transmission Electron Microscopy*. Springer, second edition, 2009.

[82] Meyer, J.C., Eder, F., Kurasch, S., Skakalova, V., Kotakoski, J., Park, H.J., Roth, S., Chuvilin, A., Eyhusen, S., Benner, G., Krasheninnikov, A.V., and Kaiser, U. Accurate measurement of electron beam induced displacement cross sections for single-layer graphene. *Phys. Rev. Lett.*, 108:196102, 2012.

[83] Warner, J.H., Schäffel, F., Zhong, G., Rümmeli, M.H., Büchner, B., Robertson, J., and Briggs, G.A.D. Investigating the diameter-dependent stability of single-walled carbon nanotubes. *ACS nano*, 3(6):1557–63, 2009.

[84] Postek, M.T. An approach to the reduction of hydrocarbon contamina-

tion in the scanning electron microscope. *Scanning*, 18(4):269–274, 1996.

[85] Dyck, O., Kim, S., Kalinin, S.V., and Jesse, S. Mitigating e-beam-induced hydrocarbon deposition on graphene for atomic-scale scanning transmission electron microscopy studies. *Journal of Vacuum Science & Technology B, Nanotechnology and Microelectronics: Materials, Processing, Measurement, and Phenomena*, 36(1):011801, 2018.

[86] Svensson, K., Jompol, Y., Olin, H., and Olsson, E. Compact design of a transmission electron microscope-scanning tunneling microscope holder with three-dimensional coarse motion. *Review of Scientific Instruments*, 74(11):4945, 2003.

[87] Wilhite, P., Vyas, A.A., Tan, J., Tan, J., Yamada, T., Wang, P., Park, J., and Yang, C.Y. Metal-nanocarbon contacts. *Semiconductor Science and Technology*, 29(5), 2014.

[88] Leng, Y. *Materials Characterization: Introduction to Microscopic and Spectroscopic Methods*. Wiley, 2013.

[89] An, L., Yang, X., and Chang, C. On Contact Resistance of Carbon Nanotubes. *International Journal of Theoretical and Applied Nanotechnology*, 1(2):1–10, 2013.

[90] Tersoff, J. Contact resistance of carbon nanotubes. *Applied Physics Letters*, 74(15):2122–2124, 1999.

[91] Karita, M., Asaka, K., Nakahara, H., and Saito, Y. In situ TEM study on changes in structure and electrical conductance of carbon nanotube-gold contact induced by local joule heating. *Journal of Materials Science*, 48(2):936–940, 2013.

[92] Agrawal, S., Raghuveer, M., Ramprasad, R., and Ramanath, G. Multi-shell Carrier Transport in Multiwalled Carbon Nanotubes. *IEEE Transactions on Nanotechnology*, 6(6):722–726, 2007.

[93] Myers, H. *Introductory Solid State Physics, 2nd Edition*. Taylor & Francis, 2003.

[94] Jiang, H., Nasibulin, A., Brown, D., and Kauppinen, E. Unambiguous atomic structural determination of single-walled carbon nanotubes by electron diffraction. *Carbon*, 45:662–667, 2007.

[95] A.A. Lucas, V. Bruyninckx, Ph. Lambien, D. Bernaerts, S. Amelinckx, J. Van Landuyt, G.V.T. Electron diffraction by carbon nanotubes. *Scanning Microscopy*, 12(3):415–436, 1998.

[96] Amelinckx, S., Lucas, A., and Lambin, P. Electron diffraction and microscopy of nanotubes. *Reports on Progress in Physics*, 62(11):1471–1524, 1999.

[97] Meyer, J.C., Paillet, M., Duesberg, G.S., and Roth, S. Electron diffraction analysis of individual single-walled carbon nanotubes. *Ultramicroscopy*, 106(3):176–190, 2006.

[98] Qin, L.C. Electron diffraction from carbon nanotubes. *Reports on Progress in Physics*, 69:2761–2821, 2006.

[99] Qin, L.C. Determination of the chiral indices (n,m) of carbon nanotubes by electron diffraction. *Phys. Chem. Chem. Phys.*, 9:31–48, 2007.

[100] Allen, C.S., Zhang, C., Burnell, G., Brown, A.P., Robertson, J., and Hickey, B.J. A review of methods for the accurate determination of the chiral indices of carbon nanotubes from electron diffraction patterns. *Carbon*, 49(15):4961–4971, 2011.

[101] Hammond, C. *The Basics of Crystallography and Diffraction*. Oxford University Press, 4th edition, 2015.

[102] Scherrer, P. Bestimmung der Größe und der inneren Struktur von Kolloidteilchen mittels Röntgenstrahlen. *Nachrichten von der Gesellschaft der Wissenschaften zu Göttingen, Mathematisch-Physikalische Klasse*, pages 98–100, 1918.

[103] Langford, J.I. and Wilson, A.J.C. Scherrer after sixty years: A survey and some new results in the determination of crystallite size. *Journal of Applied Crystallography*, 11(2):102–113, 1978.

[104] Delhez, R., de Keijser, T.H., and Mittemeijer, E.J. Determination of

crystallite size and lattice distortions through X-ray diffraction line profile analysis. *Fresenius' Zeitschrift für Analytische Chemie*, 312(1):1–16, 1982.

[105] de Keijser, T.H., Langford, J.I., Mittemeijer, E.J., Vogels, A.B.P., and IUCr. Use of the Voigt function in a single-line method for the analysis of X-ray diffraction line broadening. *Journal of Applied Crystallography*, 15(3):308–314, 1982.

[106] Cummings, A.W., Duong, D.L., Nguyen, V.L., Van Tuan, D., Kotakoski, J., Barrios Vargas, J.E., Lee, Y.H., and Roche, S. Charge transport in polycrystalline graphene: Challenges and opportunities. *Advanced Materials*, 26(30):5079–5094, 2014.

[107] Isacsson, A., Cummings, A.W., Colombo, L., Colombo, L., Kinaret, J.M., and Roche, S. Scaling properties of polycrystalline graphene: a review. *2D Materials*, 4(1):012002, 2016.

[108] Kashcheyevs, V., Tamburrano, A., and Sarto, M.S. Quantum Transport and Current Distribution at Radio Frequency in Multiwall Carbon Nanotubes. *IEEE Transactions on Nanotechnology*, 11(3):492–500, 2012.

[109] Flygare, M. and Svensson, K. Quantifying crystallinity in carbon nanotubes and its influence on mechanical behaviour. *Materials Today Communications*, 18:39–45, 2019.

[110] Flygare, M. and Svensson, K. Influence of crystallinity on the electrical conductivity of individual carbon nanotubes. *Carbon Trends*, 5:100125, 2021.

[111] Miranda, M.A.R. and Sasaki, J.M. The limit of application of the Scherrer equation. *Acta Crystallographica Section A*, 74(1):54–65, 2018.

[112] Flygare, M. and Svensson, K. Accurate determination of electrical conductance in carbon nanostructures. *In preparation for submission to Measurement Science and Technology (manuscript)*, 2021.

The influence of crystallinity on the properties of carbon nanotubes

Carbon nanotubes have been advertised as a material with quite extraordinary properties, both mechanically and electrically. The truth is that carbon nanotubes is not one material, but several different. Depending on the method used to produce them, and consequently the quality of the atomic structure within their walls, their physical properties can also differ drastically.

In this doctoral thesis a method was developed for quantifying the degree of order within the tubes' walls, namely their crystallinity, by using transmission electron microscopy. The method enables the characterization of the inherent properties of the tubes such as electrical conductivity and bending stiffness, alongside the determination of crystallinity, making it possible to quantify the influence of tube crystallinity on these critical properties. Furthermore, a model for electrical conduction in the outermost wall of multi-walled carbon nanotubes is suggested, enabling the determination of intrinsic quantities like the sheet resistance of individual crystallite grains within the walls and the boundaries in-between them.

The studies reveal a profound shift in both mechanical and electrical behavior at a critical crystallite size, with large differences connected to production method, and even between individual tubes from the same production batch. These findings successfully explain previously seen differences and highlight the need for well-defined characterization techniques with protocols and classification systems, in order to successfully exploit the promising properties of carbon nanotubes in the future.